

# Spatiotemporal variation in upper crustal seismic anisotropy and $V_P/V_S$ ratio in Groningen gas field, Netherlands: insights from shear wave splitting

Jaewoo Kim\* and YoungHee Kim<sup>✉</sup>

*School of Earth and Environmental Sciences, 1 Gwanak-ro, Gwanak-gu, Seoul 08826, Republic of Korea, E-mail: [younghkim@snu.ac.kr](mailto:younghkim@snu.ac.kr).*

Accepted 2022 September 21. Received 2022 September 2; in original form 2022 May 23

## SUMMARY

We investigated pore fluid characteristics of reservoir at the Groningen gas field, Netherlands using seismic anisotropy from shear wave splitting. We obtained 663 high-quality splitting parameters, such as delay time ( $\delta t$ ) and fast-axis direction ( $\varphi$ ), from local induced earthquakes that occurred during 2014–2020. We then conducted  $\delta t$  tomography and spatial averaging of  $\varphi$  to probe the spatiotemporal changes in the parameters. Our results demonstrate that crustal anisotropy in Groningen is closely related to changes in fluid flow and compaction of the reservoir. Low anisotropy strength (normalized delay time,  $\delta tn$ ) was detected near shut-in wells where considerable reservoir compaction has occurred, whereas high anisotropy strength occurred near operating wells with less compaction. The temporal variation in  $\delta tn$  further shows that the long-term trend is distinctly different between the shut-in and production wells: while  $\delta tn$  near the shut-in wells remained nearly constant at  $<6\text{ ms km}^{-1}$  during the entire period,  $\delta tn$  near the operating wells notably showed high values exceeding  $10\text{ ms km}^{-1}$  in 2015 and a decreasing trend until 2017. In addition to this long-term variation, short-term  $\delta tn$  variation was observed, which can be related to fluid flow perturbations owing to seasonal gas production fluctuations. The  $\varphi$  values along the NNW–SSE, WNW–ESE and E–W directions could be related to not only the *in situ* maximum horizontal stress direction but also the gas flow direction near the extraction wells. The observed negative relationship between the spatial distribution of  $P$ -to- $S$  velocity ratio and the anisotropy strength can potentially indicate that gas-filled pore spaces are dominant in the reservoir.

**Key words:** Fracture and flow; Tomography; Seismic anisotropy; Induced seismicity; Body waves.

## 1 INTRODUCTION

### 1.1 Groningen gas field

The Groningen gas field in the Netherlands (Fig. 1a) is the largest natural gas field in Europe. This colossal gas field entails a 200-m-thick and 3-km-deep gas reservoir inside an area of  $30 \times 30\text{ km}^2$  in northeast Netherlands. Continued production from the gas field since 1963 has led to reservoir compaction, resulting in overall subsidence of the region and induced seismicity (van Eck *et al.* 2006; van Eijs *et al.* 2006; van Wees *et al.* 2014; van Thienen-Visser & Breunese 2015). Induced seismicity in Groningen was first observed in the early 1990s, and its frequency and magnitude

increased until January 2014, when the Dutch government decided to reduce the gas production rate owing to growing public concerns about seismic hazards. The government closed the gas extraction wells in the central-west and northern regions of Groningen, where both the compaction and seismicity rates were high (Fig. 1b). With rapidly declining annual gas production, earthquake frequency decreased (Fig. 2). The production rate of the remaining extraction wells gradually decreased after 2014 (Fig. 3).

Because seismicity was low in northern Netherlands before 1991, the linkage between gas extraction and seismicity in Groningen has been thoroughly investigated in a number of studies. Several analytical models have been suggested for explaining the induced seismicity based on reservoir compaction. Bourne *et al.* (2018) and Bourne & Oates (2017) analytically demonstrated the Coulomb stress changes resulting from reservoir depletion. These studies suggest that factors such as pore-pressure depletion, vertical strain and topographic gradients are critical in Coulomb stress changes.

\*Now at the Department of Earth, Environmental and Planetary Sciences at Rice University.

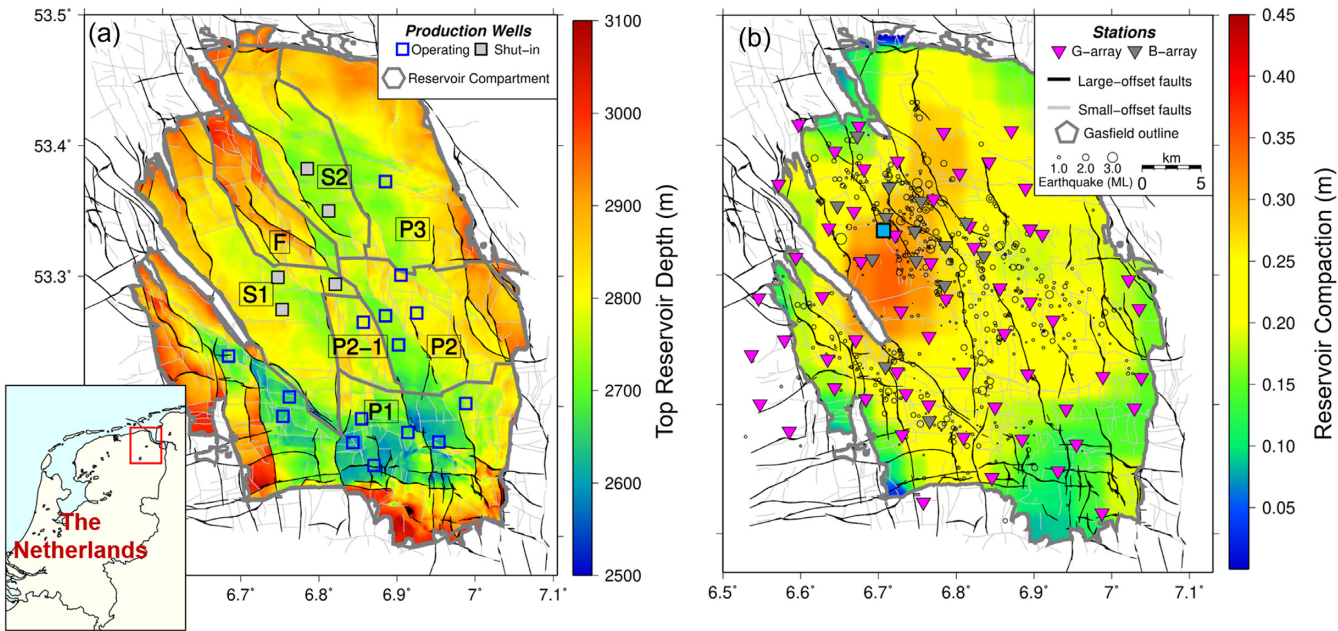


**Figure 1.** Map of Groningen gas field in Netherlands showing geological and geophysical data. (a) Map showing top reservoir depth below the gas field with the inset exhibiting our study region. The gas field is divided into several sectors; each sector is enclosed in a thick grey line with the label. Each sector includes either shut-in wells or operating wells that are shown as grey and blue squares, respectively. (b) Map showing the amount of reservoir compaction from 1960 to 2017 that is consistent with surface geodesy observations (Bourne & Oates 2017). Locations of geophones and accelerometers of KNMI (Royal Netherlands Meteorological Institute) are shown as magenta and grey triangles, respectively. Seismicity from the KNMI catalogue for the period of 2014–2019 and faults at the top of the reservoir are denoted as open circles and thin light grey lines, respectively. Location of previous shear wave splitting measurement (Zhou & Paulssen 2017) is shown as a light blue square.

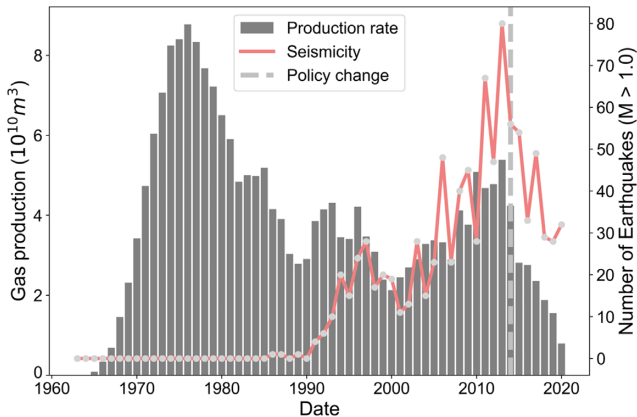


**Figure 2.** Gas production rate (Nederlandse Aardolie Maatschappij, NAM 2022) and induced seismicity in the last 60 yr at the Groningen gas field (KNMI catalogue). The number of induced earthquakes (magnitude,  $M > 1.0$ ) in the gas field is shown as a red line. The year that policy change regarding the gas production by the Dutch government is shown as a thick grey dashed line.

Dempsey & Suckale (2017) developed a seismicity model based on the Coulomb failure theory and the fracture characteristics in Groningen to forecast seismicity in the region. Moreover, faults with a large offset within the reservoir are considered a major cause of stress build-up in the reservoir (Buijze *et al.* 2017; Zbinden *et al.* 2017; van Wees *et al.* 2018).

With respect to predicting the potential impacts of gas extraction, geomechanical observations from SPG (static pressure gauge), GPS (Global Positioning System) and InSAR (Interferometric Synthetic

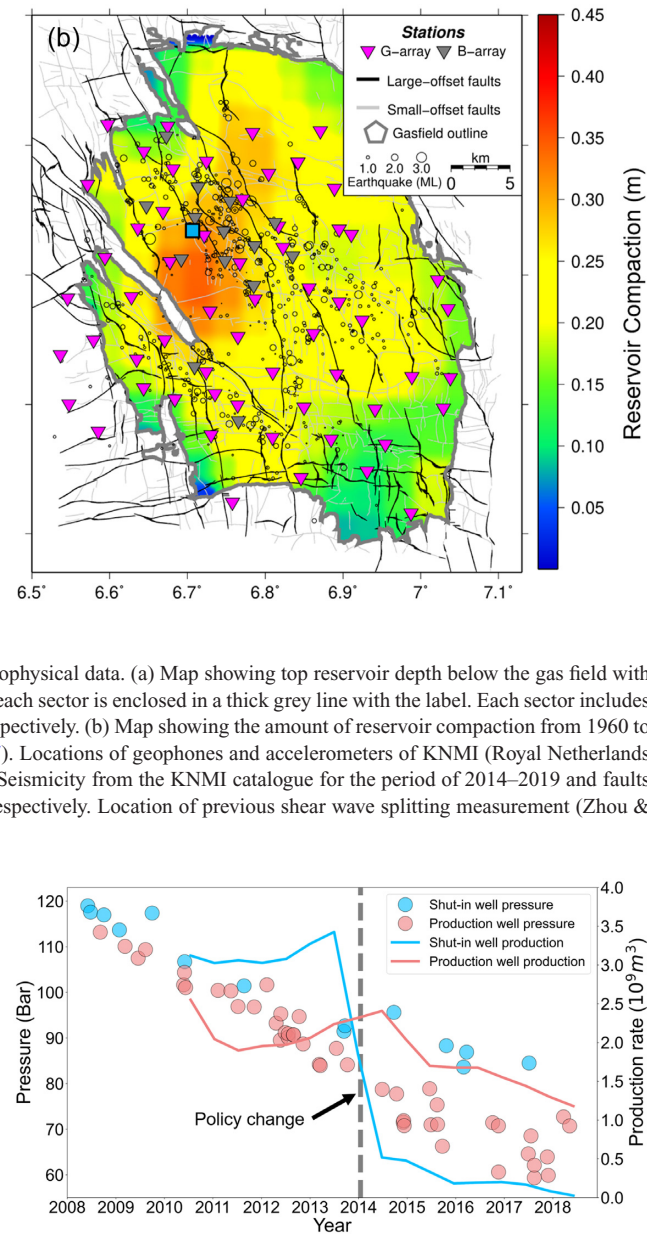


**Figure 3.** Mean reservoir pressure and average production rate of shut-in and production wells (NAM 2022). See Fig. 1(a) for the locations of the shut-in and production wells. Pressure values of the shut-in area are represented as blue circles and those of production areas as pink circles. The production rate is smoothed by 1-yr moving average and is shown as a coloured solid line. The year that production cut-down was announced is shown as a grey dashed line.

Aperture Radar) are critical for constructing feasible reservoir models (Bourne & Oates 2017; Bourne *et al.* 2018; Smith *et al.* 2019). The surface subsidence rates in Groningen based on InSAR and GPS data are inverted to estimate the compaction rate of the reservoir (e.g. Smith *et al.* 2019) and compared with the forward reservoir dynamic modelling outputs (history matching; Zeeuw & Geurtsen 2018). The reservoir pressure is generally approximated from SPG data, which amounts to 1800 measurements over 60 yr of production (van Oeveren *et al.* 2017).

Seismic arrays such as G-array, B-array and deep borehole array (NAM 2016; Dost *et al.* 2017) constructed in Groningen have

provided valuable data that led to various seismic investigations. The ability to detect and locate microseismic events improves with increasing number of sensors (Dost *et al.* 2017). Several studies using different earthquake location methods have revealed that the spatial distribution of events in Groningen adequately correlates with the distribution of faults within the gas reservoirs (Dost *et al.* 2017; Jagt *et al.* 2017; Spetzler & Dost 2017; Willacy *et al.* 2019; Smith *et al.* 2020; Willacy *et al.* 2020). Moreover, these studies have revealed that the focal depths of the events correspond closely to the depth of the reservoir, which indicates that the earthquakes are indeed induced by gas production and resulting subsidence of the reservoir. In addition, earthquake source mechanisms determined from borehole array data indicate that most of the events originate from normal fault structures (Willacy *et al.* 2019, 2020; Dost *et al.* 2020), which are known to be dominant in gas reservoir (Kortekaas & Jaarsma 2017).

Shallow velocity structures below Groningen, down to a depth of  $\sim 1$  km, have been explored in several studies using shallow borehole array data (Hofman *et al.* 2017; Kruiver *et al.* 2017; Spica *et al.* 2018a). Given that subsidence in Groningen arises from the compaction of the reservoir at a depth of  $\sim 3$  km, seismic analysis of deeper ( $>1$  km) structures is desirable. However, limited studies have been conducted on seismic structures at the reservoir level using deep borehole array data (Zhou & Paulssen 2017, 2020). Zhou & Paulssen (2020) observed that the travel times of  $P$  waves slightly decreased at the reservoir depth, which can be attributed to the reservoir compaction that occurred during the array deployment period (January to July 2015). Furthermore, Zhou & Paulssen (2017) used ambient noise interferometry to determine the  $P$ - and  $S$ -wave velocity structures of the reservoir and also conducted shear wave splitting analysis to constrain azimuthal anisotropy.

## 1.2 Crustal seismic anisotropy

Shear wave splitting (SWS) is a phenomenon whereby a  $S$  wave splits into two orthogonal components—the ‘fast’ and ‘slow’  $S$  waves—owing to their difference in velocity. This phenomenon occurs when a  $S$  wave travels through an anisotropic medium. The SWS can be quantified using two parameters: the polarized direction of the fast  $S$  wave ( $\varphi$ ) and the time lag ( $\delta t$ ) between the fast and slow  $S$  waves (Crampin 1978; Crampin & Chastin 2003).

Crustal seismic anisotropy is generally caused by (i) aligned fluid-filled microcracks (i.e. stress-induced anisotropy) and/or (ii) macroscopic structural properties (i.e. structure-induced anisotropy) such as fractures or faults (Boness & Zoback 2006). Stress-induced anisotropy is attributed to the existence of fluid-filled microcracks aligned along the direction of maximum horizontal stress  $S_{\text{Hmax}}$  (Crampin & Peacock 2008). In other words, microcracks that are not parallel to the  $S_{\text{Hmax}}$  would be considered ‘closed’, and their fluid is forced to flow into other ‘opened’ cracks. This causes the fast  $S$  wave to be polarized parallel to those opened cracks or to  $S_{\text{Hmax}}$ , while orthogonally polarized waves travel slower. Conversely, structure-induced anisotropy is often caused because crystal orientation is preferentially parallel to macroscopic features, such as pre-existing faults or folds (Llicciardi *et al.* 2018). Crustal anisotropy from local  $S$  splitting shows the alignment of the fast  $S$  wave polarization direction with the  $S_{\text{Hmax}}$  direction and/or the dominant fault direction in tectonically active or volcanic regions (Johnson *et al.* 2011; Li & Peng 2017; Hu *et al.* 2020).

Several studies have demonstrated that the SWS parameters,  $\varphi$  and  $\delta t$ , are not only related to the horizontal stress regime but also

to the pore-fluid pressure. Tang *et al.* (2005) investigated geothermal reservoirs at Krafla, Iceland, using SWS and reported significant changes in  $\delta t$  during the injection period, suggesting that SWS is an effective method for monitoring fluid pressure in cracks. Furthermore, Nolte *et al.* (2017) reported that  $\varphi$  flipped by  $90^\circ$  in the induced seismicity region such as south-central Kansas and northern Oklahoma under overpressured fluid conditions. This  $90^\circ$  flip occurs when an increase in pore pressure opens the cracks that typically remain closed due to the stress regime (Zinke & Zoback 2000; Crampin *et al.* 2004). Li *et al.* (2019) showed the temporal variation in  $\varphi$  to reveal the effect of fluid injection in hydraulic fracturing areas to understand the source of seismic anisotropy. Previous studies (Luente *et al.* 2010; Uglert *et al.* 2011) further showed that constraining  $P$ - and  $S$ -wave velocity ratios ( $V_p/V_s$  ratios) in addition to SWS parameters can provide additional useful information on reservoir properties. Mroczek *et al.* (2020) investigated the correlation between the SWS parameters and  $V_p/V_s$  ratios to infer the presence of saturated or unsaturated cracks in the reservoir and further used the  $V_p/V_s$  ratios to determine the presence of liquid- or gas-filled cracks as  $V_p$  is sensitive to gas content.

Although SWS can provide useful insights into the possible origin of anisotropy in the induced seismicity region, to date there is only one such measurement in Groningen, as reported by Zhou & Paulssen (2017). It shows that the direction of the fast axis ( $N65^\circ W \pm 18^\circ$ ) is subparallel to the direction of maximum horizontal stress, and the reservoir exhibits a fairly significant magnitude of anisotropy ( $4 \pm 2$  per cent). The measurement by Zhou & Paulssen (2017) was obtained at a single deep borehole station located in west Groningen (Fig. 1b, light blue square). In this study, we exploited the dense seismic array data in Groningen (Fig. 1b) to estimate the SWS parameters and  $V_p/V_s$  ratio to better constrain the upper-crustal seismic anisotropy in both spatial and temporal domains. Our results on crustal anisotropy were then compared with the available geomechanical data such as subsidence rate, *in situ* stress measurement and reservoir pressure in Groningen. This information is expected to provide better constraints on reservoir changes and clarify the major sources of anisotropy.

## 2 GEOLOGICAL SETTING

The Groningen gas reservoir is located at a depth of approximately 3 km within the Upper Rotliegend sandstone (Upper Permian Rotliegend Group). The thickness of the reservoir varies between 100 and 300 m. The Upper Permian Rotliegend Group is widely deposited across the region, from Western Europe (United Kingdom) to Eastern Europe (Poland) (De Jager & Visser 2017). In Groningen, the natural gas in the Rotliegend sandstone is originated from the highly faulted underlying Pennsylvanian Carboniferous limestone, which also includes coal layers (NAM 2013). The caprock of the reservoir includes the 50-m-thick Zechstein anhydrite and 0.2–1.0-km-thick halite strata (NAM 2013). Triassic claystone, Cretaceous chalk and Cenozoic North Sea formations were deposited sequentially over the caprock (NAM 2013). The reservoir and overburden layers were deposited under tectonically quiescent conditions (De Jager & Visser 2017).

Investigations based on seismic reflection, refraction, sonic logs and well-core samples have been conducted to investigate structures at various reservoir depths (down to  $\sim 3.5$  km); data from these investigations have been used to construct elastic velocity models for Groningen (Romijn 2017). 1-D  $P$ -wave velocity structures were

retrieved from the sonic log data at each well location; S-wave velocity and density structures were retrieved from the core sample data. Moreover, the data acquired from seismic reflection and refraction surveys were used to construct a 3-D velocity model of the region.

Faults within the reservoir are essential for gas production in Groningen as they can affect the pattern and speed of gas flow (NAM 2017). Approximately 1100 faults within the reservoir below the Zechstein overburden (Visser & Viota 2017) have been mapped in detail using seismic reflection and refraction surveys. Most of the faults have been identified as normal faults and are oriented in NNW–SSE directions, while some E–W and N–S trending faults are present in the southern area of Groningen (Fig. 1a; Bourne & Oates 2017; Kortekaas & Jaarsma 2017). The *in situ* maximum horizontal stress is aligned along the NW–SE direction, which is subparallel to the trending direction of the major faults and is consistent with the normal fault regime of Groningen (van Eijs 2015). Fig. 1(b) shows a clear spatial correlation between induced seismicity and fault distribution.

### 3 DATA

#### 3.1 Seismic data acquisition and preprocessing

The seismic data for our study were obtained from two borehole seismometer networks (G-array consisting of 80 geophones and a borehole network consisting of 11 geophones) and one accelerograph network (B-array consisting of 14 accelerometers). Most B-array stations were located in the west-central area of Groningen (Fig. 1b, grey triangles). Unlike the B-array, the G-array is distributed throughout the entire gas field (Fig. 1b, magenta triangles), and each station includes an accelerometer at the surface and a sequence of four geophones positioned at a vertical spacing of 50 m. In addition, we used data from 11 borehole stations in Groningen, each of which were equipped with four 4.5 Hz geophones that were placed at slightly different vertical intervals of 30–50 m (Dost *et al.* 2017). Given that the seismic energy of surface waves for local earthquakes in Groningen can decrease rapidly with depth (Spica *et al.* 2018b), we used data from the lowermost geophone, which is less affected by surface noise that can potentially disturb SWS measurements by distorting particle motions. We then corrected the orientations of the geophones using values provided by Hofman *et al.* (2017).

From January 2014 to December 2020, we collected waveforms of induced events with a positive local magnitude ( $M_L > 0$ ) to perform SWS analysis. Earthquake information was obtained from the event catalogue provided at the KNMI data portal. The event depths provided in the catalogue were fixed at 3 km, which is the average depth of the reservoir and has been validated in several previous studies (Pickering 2015; Willacy *et al.* 2019). For each station, we excluded events whose straight-line incidence angle exceeded 60°. This constraint was imposed to prevent the distortion of particle motion owing to *S*-to-*P* conversion (Booth & Crampin 1985; Savage *et al.* 2016). After this screening, we obtained 3699 event–station pairs of the data set for SWS analysis. Before conducting SWS measurements, all waveforms were bandpass filtered to improve the signal-to-noise ratio of the direct *S* waveforms. The corner frequencies of the filter were set to 1 and 20 Hz, and the background noise level was low within this range (Spica *et al.* 2018b).

#### 3.2 Pressure, compaction rate and fault offset data for the Groningen reservoir

Reservoir pressures from the SPG measurements were obtained from NAM (2022). Fault distribution and reservoir compaction data were retrieved from Bourne & Oates (2017). The fault distribution data were divided into two groups: faults with large offsets (larger than 50 per cent of the reservoir thickness) and small offsets (smaller than 50 per cent of the reservoir thickness).

The production rates of each extraction well in Groningen were retrieved from NAM (2022). In this study, wells showing rapidly decreasing production rates in/after 2014 were considered as ‘shut-in’ wells, and wells showing nearly constant production rates were considered ‘production’ wells (Fig. 1b). Thus, we divided the gas field into seven sectors, considering the locations of the production wells and the major fault lines (Fig. 1a). Sector P1 included production wells positioned in the south and had a shallow reservoir depth. Sector P2 included production wells in the central region of Groningen; in particular, the central-most region is denoted as sector P2-1, where the distribution of N–S oriented faults is dominant. Sector P3 included one isolated production well in the north and showed the least seismicity (Fig. 1b). Sectors S1 and S2, which have shut-in wells, show the largest compaction rates in the study area. We separated sector F from sectors S1 and S2 because sector F has a notably deep reservoir depth compared with those two sectors and is surrounded by large offset faults.

### 4 METHODS

#### 4.1 Splitting measurement and grading criteria

In this study we measured the SWS parameters using Pytheas code (Spingos *et al.* 2020), which provides three SWS methods: manual, eigenvalue (Silver & Chan 1991) and cluster analysis (Teanby *et al.* 2004). Among the three methods, the manual method is the least automatic method for determining the SWS parameters. This manual method yields  $\varphi$  values by manual selection of *S* arrival and rotation of the horizontal-component waveform from NS–EW to fast–slow (or  $\varphi$  parallel–orthogonal direction) (e.g. Figs S1a and b). The best  $\delta t$  value is then obtained by minimizing the time lag between the fast and slow components. To assess the quality of the best  $\delta t$ , the polarigrams and hodograms of the corrected seismogram can be used to check whether the modified particle motion is linearized (e.g. Figs S1c and d). The eigenvalue method is based on a grid search for optimal SWS parameters that generate the most linearized unsplit waveform, that is, the parameters that minimize the second eigenvalue of the covariance matrix between two perpendicular horizontal components from the selected time window (Fig. S2). Among the three methods considered in this study, cluster analysis is the most automated. This method is also based on the grid search for SWS parameters, similar to the eigenvalue method, but the grid search is repeated for slightly shifted time windows (e.g. Fig. S3). The parameter values used in the cluster analysis are listed in Table S1.

We applied several criteria to ensure consistency in the measurements by adapting the approaches used by Peng & Ben-Zion (2004) and Spingos *et al.* (2020). The criteria are as follows: (i) the signal-to-noise ratios calculated from *S* waveforms should exceed 2.0, (ii) the maximum amplitude of the horizontal component should be larger than that of the vertical, (iii) for the eigenvalue method, at

least one period of  $S$  wavelet should be included within the window, (iv) the absolute correlation coefficient between the corrected ‘fast’ and ‘slow’ component traces should be greater than 0.6 ( $CC_{NE\min}$ ), (v) the standard deviations of  $\varphi$  and  $\delta t$  should be lower than  $20^\circ$  ( $\delta\varphi_{\max}$ ) and 20 ms ( $\delta t_{d\max}$ ), respectively and (vi) the difference between  $\varphi$  and initial polarization angle ( $p$ ) should exceed  $15^\circ$  and less than  $75^\circ$ . Criteria (iv) and (v) were applied to the data for the eigenvalue and cluster analysis methods. The parameters that did not fulfil the (i)–(v) criteria were given an ‘E’ grade; the parameters that did not satisfy the criterion (vi) were assigned the ‘N’ (null) grade. The remaining data were allocated to ‘A’, ‘B’ and ‘C’ grades based on the normalized score ( $S$ ) of the correlation coefficient of two horizontal components ( $CC_{NE}$ ) and the standard deviation of SWS parameters ( $\delta t_d$  and  $\delta\varphi$ ). The  $S$  can be computed using the following equation:

$$S = \frac{\frac{\delta\varphi}{\delta\varphi_{\max}} + \frac{\delta t_d}{\delta t_{d\max}} + \frac{1 - |CC_{NE}|}{1 - |CC_{NE\min}|}}{4} \quad (1)$$

where the max and min are the maximum and minimum values allowed for criterion (v), respectively. In the case of the manual method, we graded the parameters based on a visual inspection of the hodogram and polarigram that shows the ellipticity of the particle motion before and after the correction. Quality ‘A’ and ‘B’ measurements include data set showing that corrected particle motion pattern is linear or close to linear.

The two automated methods for SWS have advantages in terms of measurement speed while reducing user bias. However, these methods can potentially yield erroneous results owing to cycle skipping (e.g. Johnson *et al.* 2011; Castellazzi *et al.* 2015). Cycle skipping is a phenomenon that makes  $\delta t$  have a large uncertainty (half of a period length) when the pre- $S$ -phase is not included in the time window or when several cycles of the wave are included in the time window (Savage *et al.* 2010, 2016). Thus, we rejected pairs that showed inconsistencies in both the quality and quantity of the parameters. More specifically, we discarded event–station pairs that had a circular standard deviation of  $\varphi$  greater than  $20^\circ$  and a standard deviation of  $\delta t$  greater than 5 ms (Fig. S4). We rejected the pair even if one of the parameters was graded lower than ‘B’ grade. For the final SWS parameter data set, we used values from the manual method because this method involves a visual assessment of the data.

We observed that each method can yield different grades when the parameters are close to the threshold value of the null criterion ( $|p - \varphi| \approx 15^\circ$  or  $75^\circ$ ). Fig. S5 shows examples of these null measurements. To increase the robustness of the measurement, we assigned ‘N’ grade to the parameters in the case when ‘N’ grade is assigned for one method while different grades for other methods. We designate this case as ambiguous null; the robust null is obtained when two methods output ‘N’ grade.

#### 4.2 $\delta t$ tomography and spatial averaging of $\varphi$

Using the splitting parameters, we exploited the program called TESSA (Tomography Estimation of Shear wave splitting and Spatial Averaging; Johnson *et al.* 2011) to perform 2-D  $\delta t$  tomography inversion and spatial averaging of  $\varphi$ . TESSA provides both the quadtree gridding method (Townend & Zoback 2001, 2004) and regular gridding method for the  $\delta t$  tomography and spatial averaging of  $\varphi$ . The quadtree gridding method is effective for the study region with an unevenly distributed ray density, as in our study, but several input parameters for gridding must be predefined. Gridding

is performed iteratively with respect to the maximum and minimum number of rays per cell and the minimum cell size (Townend & Zoback 2001, 2004).

We adopted the quadtree gridding method to grid our study area using the full event catalogue because the earthquake epicentres and stations were not equally distributed in Groningen (Fig. S6c). For temporal comparison using 3-yr catalogues, we used the regular gridding scheme such that the grid size remained the same for all time intervals, which allowed to compare the inversion results in a spatially consistent manner. The parameters of the quadtree gridding schemes are listed in Table S2.

After gridding, we conducted tomographic inversion of  $\delta t$  using TESSA. The basic scheme of the method is that  $\delta t$  is cumulatively added to the splitting times along the ray path, which provides a first-order approximation to the heterogeneous anisotropic structure of the study area (Johnson *et al.* 2011). Because the delay time is accumulated along the ray path as the  $S$  wave splits, we normalized the  $\delta t$  with the straight-line path distance, and this quantity is denoted as  $\delta tn$  representing the strength of anisotropy (e.g. Johnson *et al.* 2011; Cao *et al.* 2019). Using the full catalogue, 661 ray paths from 75 stations and 403 events were used in the inversion. The residual norm for the inversion converged to 0.0769 after nine iterations.

To estimate the resolution of the final output model from the inversion, a synthetic checkerboard resolution test was performed. In this test, we constructed an input model with alternating patterns of high and low values for the strength of anisotropy (20 and 10 ms km<sup>-1</sup>, respectively) with random noise from a standard normal distribution (Fig. S6a). The inversion reduced the residual norm to 0.0016 after eight iterations. Fig. S6(b) illustrates recovered checkerboard anomalies. Poorly recovered regions with residuals larger than 0.002 s km<sup>-1</sup> are masked in grey and excluded from the interpretation (Fig. S6d).

In addition to providing single-station results of  $\varphi$  for each station in Groningen from the three SWS methods, we spatially averaged  $\varphi$  for each grid cell in a circular statistical manner (e.g. Johnson *et al.* 2011). We tested six weighting schemes to determine the optimal weighting factors for each grid, which resulted in the least scattered distribution of  $\varphi$ . TESSA provides four weighting schemes by default: (1) no weighting, (2)  $1/D$ , (3)  $1/D^2$  and (4)  $\delta t$  tomography, where  $D$  is the distance from the grid cell to the station (Audoine *et al.* 2004). We adjusted the default schemes and applied two additional schemes considering our study region where dense seismic networks are available in relatively localized areas. Considering the relatively short event–station distances owing to shallow focal depths, we used  $d_{st}$  rather than  $D$  for the distance from the node to the station. The additional weighting schemes are (5)  $1/d_{ev}$  and (6)  $1/d_{ev}^2$ , where  $d_{ev}$  is the distance from the node to the epicentre. We then weighted each node of the ray path with each weighting scheme and obtained an average for each grid cell. The results were excluded if the standard deviation of  $\varphi$  in the grid cell exceeded  $25^\circ$ .

#### 4.3 Estimating $V_p/V_s$ ratio

We further calculated the average ratio of  $V_p$  and  $V_s$  along the ray path of each event–station pair to examine the correlation between the SWS parameters and  $V_p/V_s$  ratio at spatial and temporal scales. Assuming homogenous  $V_p/V_s$  along the linear ray path, the  $V_p/V_s$  ratio of each event–station pair can be computed as follows:

$$\frac{V_p}{V_s} = \frac{d/T_p}{d/T_s} = \frac{T_s}{T_p} \quad (2)$$

where  $d$  is the ray path length, which is assumed to be identical for the  $P$  and  $S$  waves, and  $T_p$  and  $T_s$  are the traveltimes of the  $P$  and  $S$  waves, respectively. We note that the station depth varies between 0 and 200 m in our study region, and that the sediment layer in this depth range can have a substantially high  $V_p/V_s$  ratio ( $\sim 4.5$ ; Hofman *et al.* 2017; Romijn 2017). Thus, we applied a correction to minimize the discrepancy in  $V_p/V_s$  ratio from the data recorded from surface accelerometers and borehole geophones (Fig. S7a). We assumed a constant velocity structure between 0 m and 200 m depth to calibrate  $V_p/V_s$  ratio for stations positioned at depths shallower than 200 m. The  $V_p/V_s$  ratio, including the calibration terms, is shown as

$$\frac{V_p}{V_s} = \frac{T'_s - \frac{z'}{v_s}}{\frac{T'_p - \frac{z'}{v_p}}{T_p - \frac{z'}{v_p}}} \quad (3)$$

where  $z'$  represents the vertical distance from a depth of 200 m, and  $v_p$  and  $v_s$  are the average  $P$ - and  $S$ -wave velocities of the subsurface, respectively. Fig. S7(b) shows the results of  $V_p/V_s$  after the correction. We only showed the  $V_p/V_s$  values between 1.5 and 2.6, because values beyond this range may not be realistic, according to the velocity model for Groningen (Romijn 2017).

Several assumptions have been made to decipher the observed  $V_p/V_s$  variations in Groningen, which can be related to variations in reservoir features. First, we assumed that the distribution of the epicentral distances was nearly uniform in our study area. Because the ray path travels deeper layers longer as the epicentral distance increases, the average  $V_p/V_s$  ratio from a farther epicentral distance is closer to the  $V_p/V_s$  ratio of the deeper layers. Hence, we ensured that the distribution of epicentral distances was not disparate when we compared the mean  $V_p/V_s$  ratios of the two different regions. Second, we presume that the thickness of each layer is constant or fluctuates randomly in the study area. Zechstein salt, which sits on top of the reservoir, is known to have a strong variation in thickness (Willacy *et al.* 2019). Thus, we only considered  $V_p/V_s$  ratios in the region where the thickness of the Zechstein salt is more or less constant compared with the southwest or northeast of Groningen (Fig. S14c).

#### 4.4 Applying moving window average

To display the parameter values for each event–station pair to detect their temporal changes, we applied a moving window average technique to minimize the scatter in the values. We used a moving mean filter of 100 d, with a step interval of 13 d. For each window, we estimated 95 per cent confidence intervals using the non-parametric bootstrap method. Bootstrapping was performed using randomly sampled parameters in each moving window. After 1000 iterations of bootstrap resampling, we defined a 95 per cent confidence interval (CI) from 2.5 to 97.5 per cent of the sample in each window.

## 5 RESULTS

High-quality 1922 SWS parameter values were obtained from 3699 waveforms recorded from 76 stations in Groningen. Among these parameter values, 663 event–station pairs yielded either A or B grades in all three splitting methods, and 665 pairs yielded well-constrained nulls. For  $V_p/V_s$  ratios, we manually picked  $P$ -wave arrivals for each event–station pair and used  $S$  arrivals obtained from the SWS measurement regardless of the grades from the SWS methods. The 1798 event–station pairs with measured  $P$  and  $S$  arrival times were then used to compute the  $V_p/V_s$  ratios. In subsequent

sections, we report the spatial and temporal variations in the delay time  $\delta t$ , fast polarization direction  $\varphi$  and  $V_p/V_s$  ratio.

### 5.1 Spatial distribution of $\delta t$ , $V_p/V_s$ ratio and null proportion

The  $\delta t$  varies from 5 to 75 ms in our study area with an average of  $20.0 \pm 11.2$  ms; the  $\delta tn$  then varies from 1.07 to  $19.99 \text{ ms km}^{-1}$  with an average of  $4.9 \pm 2.6 \text{ ms km}^{-1}$  (Fig. S9). The  $\delta tn$  value for each station can be compared with two related reservoir properties: the topographic gradient of the top reservoir and the compaction of the reservoir. The topographic gradient with the fault offset at the reservoir and uneven reservoir compaction rates are regarded as the major contributing factors in inducing seismicity in Groningen (van Wees *et al.* 2014; Buijze *et al.* 2017; Zbinden *et al.* 2017).

The region with the largest compaction rate and the lowest topographic gradient displayed lower  $\delta tn$  ( $< 6 \text{ ms km}^{-1}$ ), whereas the surrounding areas with somewhat larger topographic gradients showed higher  $\delta tn$  ( $> 6 \text{ ms km}^{-1}$ ; Fig. 4a). The 2-D tomography of  $\delta tn$  also shows a distribution similar to that shown in Fig. 4(a); however, small-scale heterogeneities of  $\delta tn$  values become more evident in the north-central part of the gas field (Fig. 4b). Although the spatial resolution for 2-D tomography is very limited, the low strength of anisotropy in the northeast area of the gas field corresponds to the area of a small topographic gradient (Fig. 4).

As Fig. 5 shows, both  $V_p/V_s$  ratio and null proportion at each station showed similar spatial distributions; however, both showed patterns contrasting to the distribution of  $\delta tn$  (Fig. 4b). Most of the lower values of both  $V_p/V_s$  ratio ( $< 2.1$ ) and null proportion ( $< 0.5$ ) appear in the southern and southeastern areas where higher  $\delta tn$  is observed (Fig. 4b).

### 5.2 Temporal distribution of $\delta tn$

Fig. S9 shows the temporal variation in  $\delta tn$  for the entire period considered in this study. We observed that the change in  $\delta tn$  is evident in terms of its mean value and confidence interval (Fig. S9, red solid line and dashed lines, respectively). In 2015,  $\delta tn$  had the largest rolling mean value of  $7.36 \text{ ms km}^{-1}$  ( $\pm 1.99 \text{ ms km}^{-1}$  confidence interval). Its value then gradually decreased until 2017 with a minimum rolling mean value of  $3.99 \text{ ms km}^{-1}$  ( $\pm 0.41 \text{ ms km}^{-1}$  confidence interval). After 2017, an increase of  $\delta tn$  was observed, and in 2020 the maximum rolling mean value of  $6.37 \text{ ms km}^{-1}$  ( $\pm 1.46 \text{ ms km}^{-1}$  confidence interval) was achieved.

Although the amount of gas production continuously decreased during the entire period, it is somewhat difficult to find a definitive correlation between the gas production and delay time because the production wells are not evenly distributed in the gas field. We thus examined the temporal variation in different areas that were subdivided according to well production status and bounded by large-offset faults (Fig. 6c).

Figs 6a and b show temporal variations in  $\delta tn$  for the shut-in well and production well clusters (Fig. 6c), respectively; the two indeed showed different trends. The shut-in well cluster showed no significant long-term increase or decrease in  $\delta tn$ , but its rolling mean value fluctuated from a minimum of  $2.67 \pm 0.03 \text{ ms km}^{-1}$  to a maximum of  $6.19 \pm 1.00 \text{ ms km}^{-1}$  (Fig. 6a). Conversely, from 2014 to 2017, the production well cluster showed a notable decreasing trend in both the mean value and deviation of  $\delta tn$  (Fig. 6b). In this 4-yr period, the rolling mean value ranged from a maximum of  $9.72 \pm 4.25 \text{ ms km}^{-1}$  to a minimum of  $3.68 \pm 0.80 \text{ ms km}^{-1}$ ; a slight

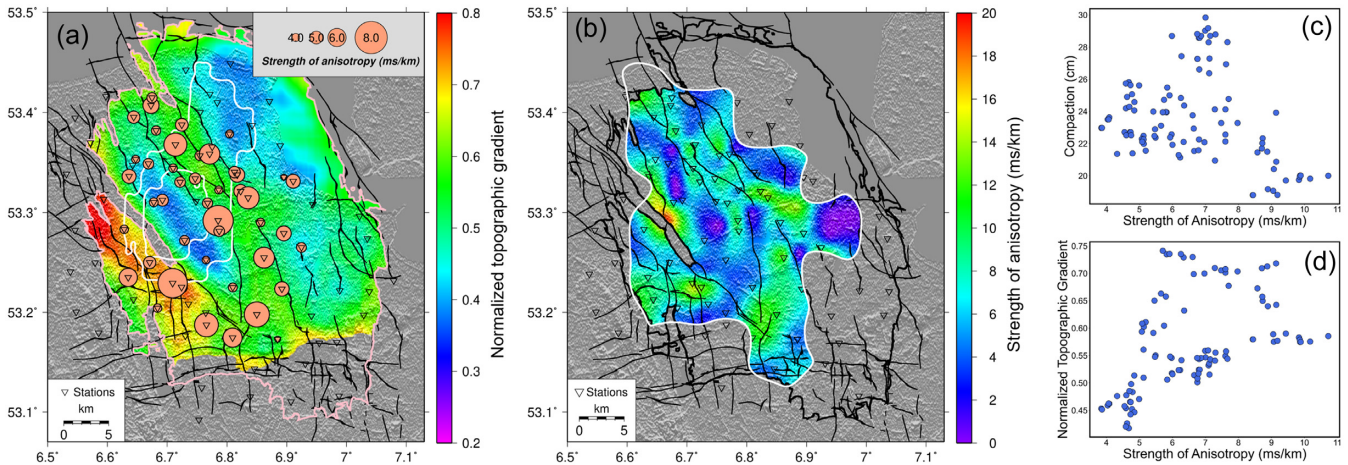


**Figure 4.** Strength of seismic anisotropy in two different views. (a) Map showing the strength of anisotropy averaged at each station (at least 5  $\delta tn$  are measured). Background colours represent normalized topographic gradients of the top reservoir surface (Bourne & Oates 2017). White contour lines enclose two areas showing large compaction in the gas field (inner: 0.3 m, outer: 0.25 m). (b) Tomography result of  $\delta tn$ . Black lines represent fault lines that have large offsets (exceeding 50 per cent of the reservoir thickness) at the top of the reservoir (Bourne & Oates 2017). (c) Correlation between strength of anisotropy and reservoir compaction in the gas field. (d) Correlation between strength of anisotropy and normalized topographic gradient of the top reservoir surface.

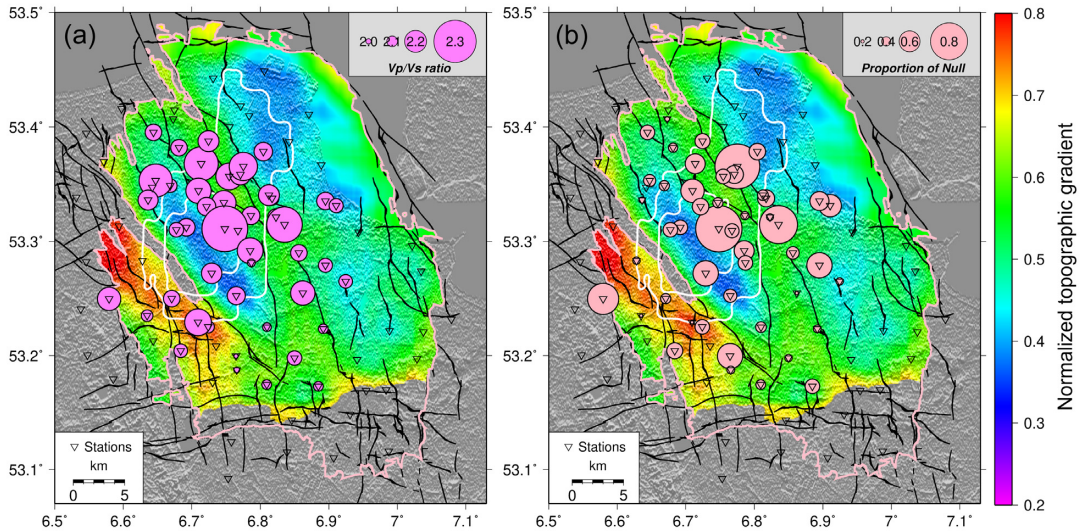


**Figure 5.** Maps showing (a)  $V_p/V_s$  ratio averaged at each station (at least 15 measurements of  $V_p/V_s$  ratio included) and (b) null proportion in each station (at least 10 measurements included). White contour lines enclose two areas showing large compaction in the gas field (inner: 0.3 m, outer: 0.25 m).

increase of  $\delta tn$  was observed in 2019 and 2020 (Fig. 6b). Short-term fluctuations of  $\delta tn$  in both the shut-in well and production well clusters correlated well with the monthly gas production rate of the production well cluster (Figs 6b and b, grey solid line). Furthermore, high values of  $\delta tn$  at the shut-in well cluster (Fig. 6a, black arrows) were observed in winter when the production rate increased at the operating wells.

### 5.3 Spatial variation of $\varphi$

The  $\varphi$  assigned with A or B grade were mostly aligned in two predominant directions: N70°W–N50°W and N20°W–N10°E, corresponding to the distribution of fault strikes at the reservoir (Fig. 7). Furthermore, the  $\varphi$  values were generally aligned with the maximum horizontal stress directions, as derived from *in situ* stress measurements at the reservoir, and the dominant direction of N60°W–70°W was parallel to the fast-axis direction measured by Zhou & Paulssen

(2017). Null measurements were mostly in the range of N40°E–N70°E (Fig. 7), nearly perpendicular to the distribution of the  $\varphi$ , which suggests that a large proportion of the nulls represent the slow-axis direction.

In Figs 8 and 9, we superimposed three notable references of the maximum horizontal stress directions that can be compared against the spatial variation in  $\varphi$ : one SWS measurement from the deep borehole (Zhou & Paulssen 2017; pink double-headed arrow in Fig. 8), four *in situ* stress measurements (van Eijs 2015; light-blue double-headed arrows in Fig. 8), and 13 fault orientations determined from the focal mechanism solutions (Dost *et al.* 2020; green double-headed arrows in Fig. 8). Fig. 8 presents the  $\varphi$  and null directions for each station that were constrained from more than 10 measurements. The  $\varphi$  values from stations in sectors S1 and P1 are oriented in the NW–SE or N–S direction, which align well with the maximum horizontal stress direction (Fig. 8a). The  $\varphi$  from sector P2–1 shows a robust ENE–WSW direction (Fig. 8a).

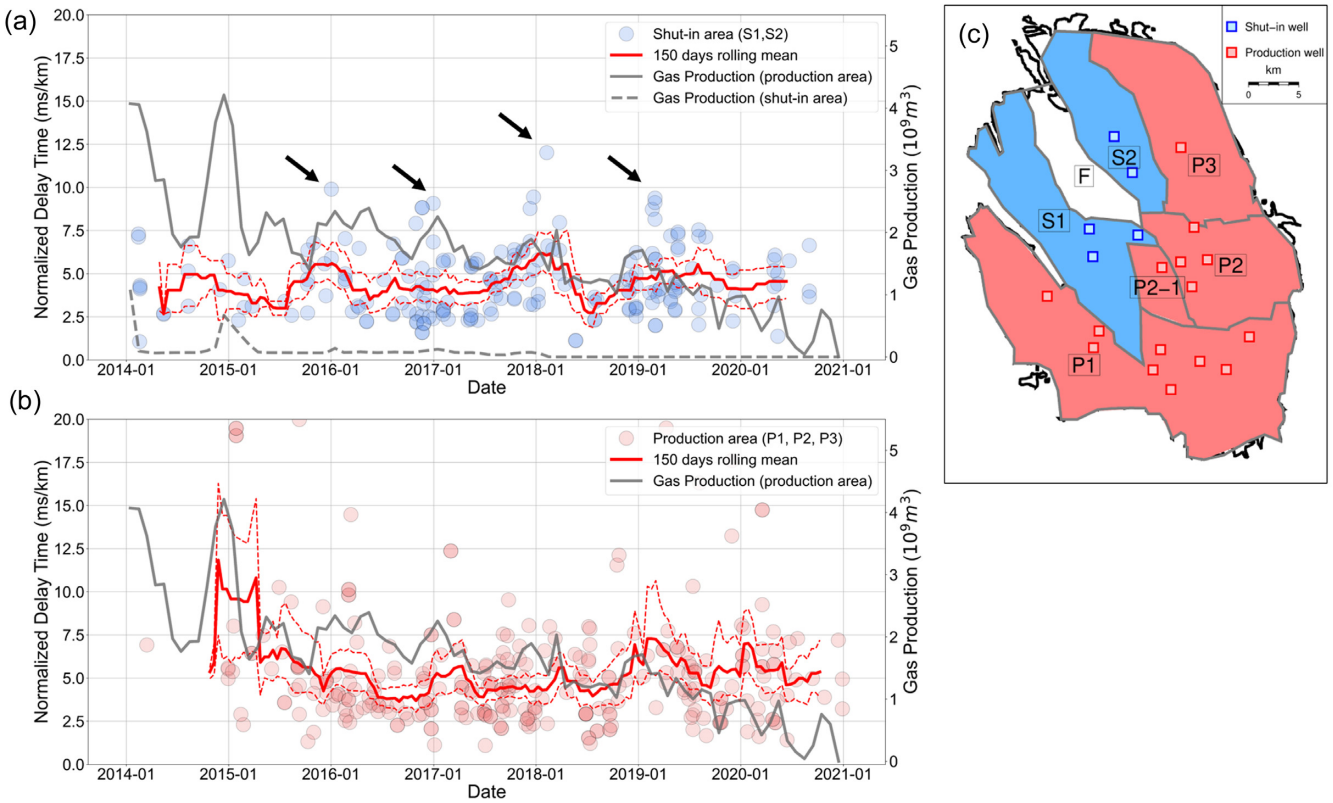


**Figure 6.** Temporal variation of  $\delta tn$  from 2014 to 2020 at two regions: (a) shut-in well cluster and (b) production well cluster. (c) Compartmentation of the study area by locations of wells and large offset faults. Light blue circles in (a) indicate measured values of  $\delta tn$  for sectors S1 and S2. Light pink circles in (b) represent measured values of  $\delta tn$  for the sectors P1, P2 and P3. Red solid lines in (a) and (b) indicate a 100-d moving mean value with a 13-d step, and red dashed lines for 95 per cent confidence interval. The grey solid lines in (a) and (b) indicate monthly gas production in production well cluster, and the grey dashed line in (a) presents monthly gas production in shut-in well cluster (NAM 2022). Black arrows in (a) indicate the high  $\delta tn$  in winter season.

Sector F includes stations with  $\varphi$  observation that are parallel to the reference stress directions, but some stations show directions perpendicular to the reference directions (Fig. 8a). Several stations from the sectors S1, P2 and F show somewhat large variation in  $\varphi$  (Figs S10 and S11). On the other hand, the null directions in sectors S1, S2 and P3 are consistently aligned in the ENE–WSW direction, while those in sectors F and P1 are highly scattered (Fig. 8b). In particular, nulls from stations in sector P1 show bimodal NW–SE and NE–SW directions (Fig. 8b).

Because the stations were not evenly distributed in our study area, we applied the spatial averaging method, and Fig. S8 shows the results of the spatial averages of  $\varphi$  based on the six weighting schemes. Among the results obtained for the different weighting schemes considered, we selected the weighting scheme that gives rise to the least scattered measurements. As a result, the scheme with a weight of  $1/d_{ev}^2$  yielded the highest number of grid cells meeting the criteria (81 out of 103 cells), while 61 ‘less-scattered’ grid cells were obtained with no weighting, 72 with a weighting of  $1/d_{st}$ , 74 with a weighting of  $1/d_{st}^2$ , 66 with  $\delta t$  tomography and 73 with a weighting of  $1/d_{ev}$  (Fig. S8). This result indicates that the value of  $\varphi$  was highly affected by the subsurface layer near the hypocentre.

The spatially averaged  $\varphi$  from the weighting scheme of  $1/d_{ev}$  (Fig. S8f) was generally aligned with the regional stress directions (Fig. 9). Specifically, the  $\varphi$  from sector P1 and northwest of sector S1 show N–S to NW–SE directions, which are subparallel to the reference stress directions, whereas the  $\varphi$  from sectors P2, P2-1, P3

and east of S1 mostly show E–W directions (Fig. 9). Finally, the  $\varphi$  from sectors F and S2 show inconsistent directions; the central region of sectors F and S2 show a NW–SE direction, which is parallel to the stress references, whereas the northern part of F and S2 shows an N–S direction, and several directions are oriented along the NE–SW direction perpendicular to the stress direction (Fig. 9).

## 6 DISCUSSION

### 6.1 Strength of anisotropy in the Groningen reservoir

Because each seismic ray travels through not only the reservoir but also the upper geological structures, it is necessary to evaluate the contribution of reservoir anisotropy to the total strength of the anisotropy. In this regard, we compared the strength of anisotropy with SWS measurement at the reservoir depth level, which was conducted by Zhou & Paulssen (2017). Zhou & Paulssen (2017) reported that the magnitude of anisotropy in the layer between the top and bottom (2809–3017 m) of the reservoir was  $4 \pm 2$  per cent, which we converted to a  $\delta t$  of  $3.6 \pm 1.8$  ms using the average S-wave velocity of  $2225 \text{ m s}^{-1}$  at the reservoir (Romijn 2017). Considering that the average  $\delta t$  value obtained from nearby ( $< 3$  km) earthquakes was  $12.3 \pm 6.1$  ms, the reservoir contributes to  $\sim 30$  per cent of the delay time along the overall ray path and can be considered highly anisotropic.

As crustal anisotropy is generally attributed to two elements, stress-aligned fluid-filled microcracks and macroscopic structures

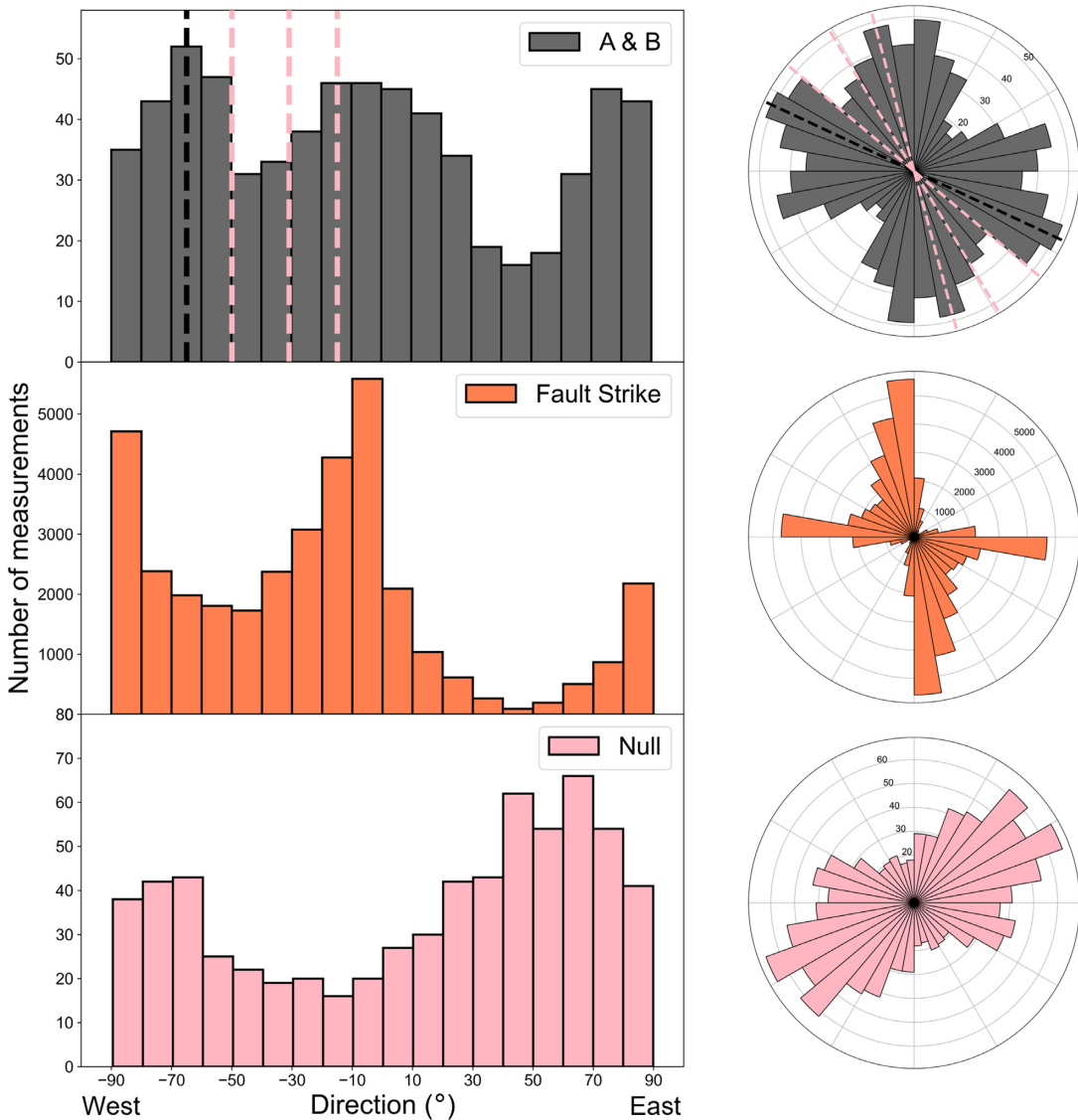


**Figure 7.** Distribution of  $\varphi$  and fault orientation (strike) illustrated with bar plot (left-hand side) and rose diagram (right-hand side). Grey bins indicate  $\varphi$  values that are graded as A and B, orange bins represent fault strikes at the top reservoir (Bourne & Oates 2017) and pink bins represent the number of null grades. Black and pink dashed lines indicate  $\varphi$  measured by Zhou & Paulsen (2017) and maximum horizontal stress directions of the gas field (van Eijs 2015), respectively.

(Boness & Zoback 2006; Crampin & Peacock 2008), the anisotropy in Groningen can be attributed to the pore fluid in the reservoir and the overburden, as well as to the mineral alignment of the faults in the reservoir. It is indeed difficult to precisely distinguish the two elements for the source of anisotropy in Groningen because the faulting stress region in Groningen is known to have a normal fault regime (Willacy *et al.* 2019; Dost *et al.* 2020), which makes the fault orientation generally parallel to the maximum horizontal stress direction.

Nevertheless, there are a number of evidences that suggest that the dominant source of crustal anisotropy in Groningen is likely to be stress-aligned fluid-filled microcracks. First, we observed that the  $\delta tn$  varied considerably in Groningen (Fig. S9). The temporal variation in the delay time generally provides meaningful insights that can help distinguish the presence of stress-induced anisotropy from structure-induced anisotropy. Although the strength of the

structure-induced anisotropy does not fluctuate over time, the stress-induced anisotropy in terms of its magnitude and direction can vary with time as the active stress field changes (Pastori *et al.* 2019). Secondly, the observed lower strength of anisotropy in the central-northern area, which is a highly faulted area in Groningen (Fig. 4), indicates that structure-induced anisotropy can be limited. In addition, notable temporal changes in  $\delta tn$  imply a substantial contribution from stress-induced anisotropy.

Our analysis results show that the strength of anisotropy varied substantially over 6 yr both spatially and temporally. As shown in Fig. 4,  $\delta tn$  spatially correlates with the topographic gradient of the top reservoir and its compaction rate. In Figs 4(c) and d, we sample 100 grid points in Fig. 4b to quantitatively compare  $\delta tn$  with topographic gradient and reservoir compaction rate. We found that  $\delta tn$  has a negative correlation (correlation coefficient of  $-0.29$ ) with reservoir compaction and a positive correlation (correlation coeffi-

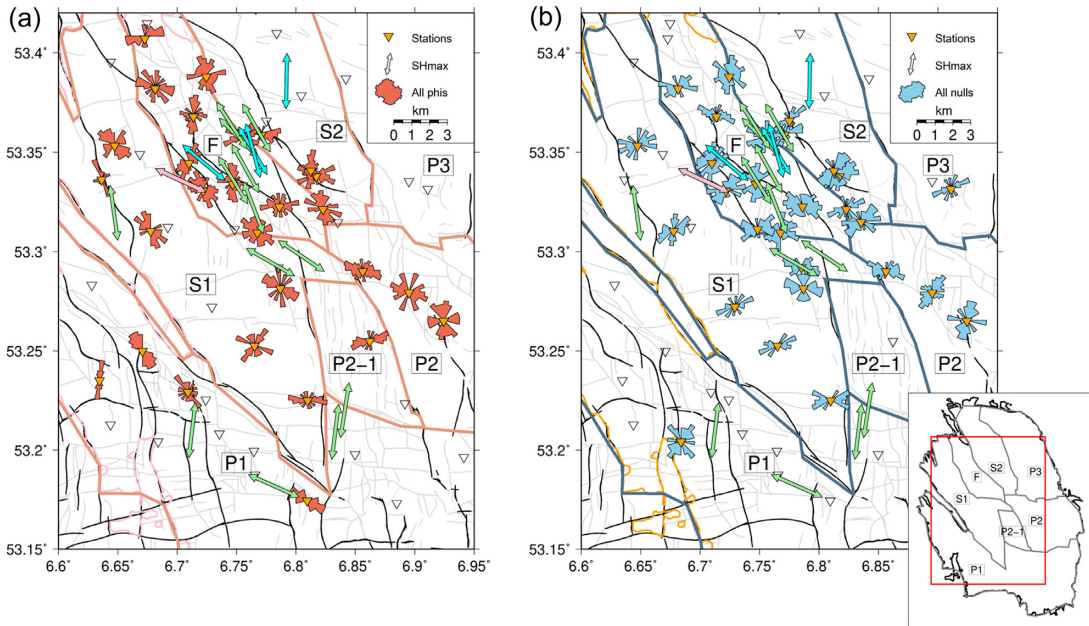


**Figure 8.** Histogram of (a)  $\varphi$  and (b) null directions for each station. Results from the stations that have less than 10 measurements are not shown. Double-headed arrows indicate maximum horizontal stress directions measured by previous studies (pink: Zhou & Paulsen 2017, light blue: van Eijs 2015, green: Dost *et al.* 2020) that can be compared against our measured directions. Black lines represent fault lines that have large offsets (exceeding 50 per cent of the reservoir thickness) at the top of the reservoir (Bourne & Oates 2017). Light grey lines indicate faults with small offsets (Bourne & Oates 2017). See Figs S10 and S11 for enlarged figures.

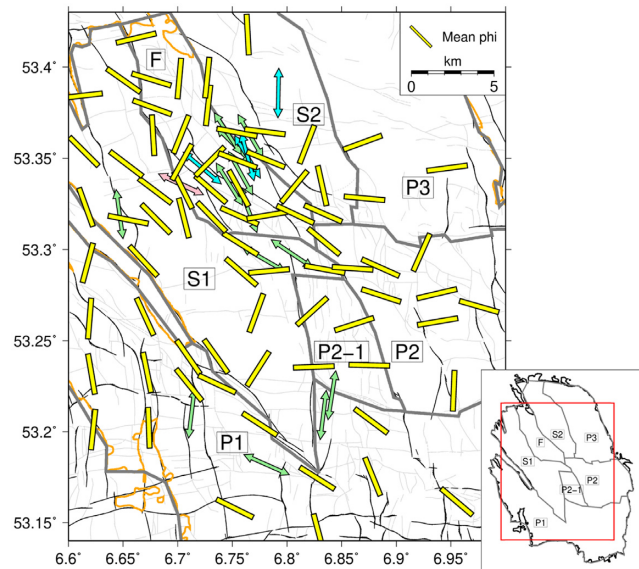


**Figure 9.** Spatially averaged  $\varphi$  for all A and B graded data sets. Yellow bar indicates the circular mean value of  $\varphi$  in each grid. Double-headed arrows indicate maximum horizontal stress directions as reference (pink: Zhou & Paulsen 2017, cyan: van Eijs 2015, green: Dost *et al.* 2020).

cient of 0.49) with topographic gradient. Therefore, we interpret that the observed low strength of anisotropy in the west-central area was a consequence of reservoir compaction. When gas escapes from the pore spaces, a significant number of microcracks are closed, which can lead to a decrease in the strength of anisotropy. Consequently, the high  $\delta tn$  in the south to the east-central areas of the gas field (Fig. 4) can be attributed to the presence of overpressurized pore fluids or additional microcracks at the reservoir. Densely populated

large-offset faults may control fluid flow such that pore fluid overpressure can develop at the reservoir. The microcracks can then be reopened owing to the fluid flow near the extraction wells (Fig. 10).

As demonstrated in Fig. 6, the discrepancy in the observed long-term trend of  $\delta tn$  at both the shut-in well and production well clusters can be related to the amount of gas production in Groningen. Assuming that nearly no gas production was conducted in the shut-in area, there should be negligible variation in the pore-fluid pressure, leading to a nearly constant strength of anisotropy over time. However, continued gas extraction in the production area could lead to a decrease in pore pressure, resulting in a decreasing trend in  $\delta tn$ .

Fig. 6 further shows short-term (or seasonal)  $\delta tn$  peaks in both the shut-in and production well clusters, and the peaks in both clusters correlate adequately with the overall gas production rate (Fig. 6, grey solid line). This production-related short-term variation in anisotropic strength implies that a sharp increase in gas production temporarily strengthens the pressure gradient and fluid flow towards the extraction well, leading to additional opening of microcracks in the direction of the fluid flow. Hence, the four observed distinct peaks of  $\delta tn$  in the shut-in well cluster might be caused by fluid flow from the shut-in well cluster to the nearest active wells within the production well cluster (Fig. 10).

Fig. 10 illustrates a schematic view of the fluid flow-related changes in seismic anisotropy based on our seismic observations in Groningen. When gas production temporarily increases in the winter season, active fluid flow can be expected not only in the area near the operating wells in the southeast region but also in the northwest region where the shut-in wells are located. This flow may cause the alignment of the microcracks to become more parallel to the direction of the flow, thus creating a medium with a higher degree of seismic anisotropy. When gas production decreases in the summer season, active fluid flow is only present near the production well cluster; this results in a smaller anisotropic strength

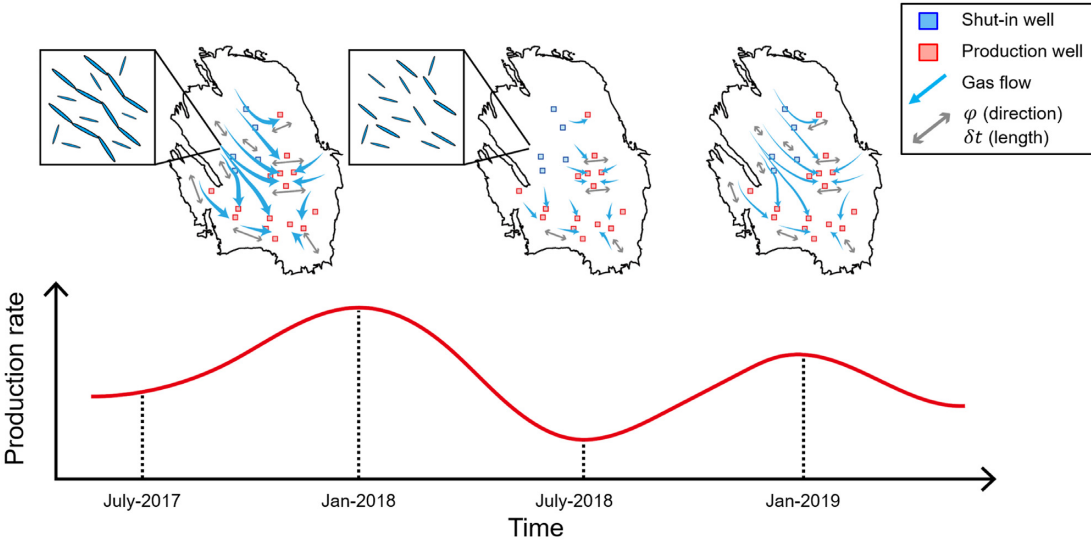


**Figure 10.** Schematic diagram showing strength and directions of gas flow according to the temporal changes in gas production rate, inferred from the variations in the strength of anisotropy and fast axis directions observed in this study.

in the northwest region, while a moderate strength of anisotropy is maintained in the southeast region. On this basis, the lower strength of anisotropy during the overall period is spatially limited in the shut-in well cluster, whereas higher values are present only in the production well cluster.

## 6.2 Local stress regime and direction of fluid flow in Groningen

In tectonically active regions, the crustal anisotropy can be primarily caused by the alignment of the fast  $S$ -wave polarization direction with the maximum horizontal principle compressive stress direction and/or the dominant fault direction. However, it is not only related to fault direction, but strictly parallel to the fault strike only if the station is present on the fault (Cochran *et al.* 2006; Gao *et al.* 2011). In Groningen, as Fig. 11 shows, several  $\varphi$  values obtained from the regions closest to the fault show values parallel to the fault strike and with some deviations. This might stem from the discrepancy between fault depth (3000 m) and station depth (200 m), which causes seismic ray geometry not passing through the fault. In other words, the local stress regime or/and pore pressure might contribute to our observed fast axis directions in Groningen.

Although the distribution of our fast-axis directions is spatially complex in Groningen, we observed two dominant directions oriented in the NW–SE and EW directions (Fig. 9). The NW–SE oriented  $\varphi$  appeared on the west side of the gas field (sectors P1, S1 and F), whereas the EW-oriented  $\varphi$  appeared on the east side of the gas field (sectors P2-1, P2 and P3). Although the reference  $S_{H\max}$  values were mostly aligned in the NW–SE direction, no reference values existed on the east side of the gas field. Thus, we expect sectors P2-1, P2 and P3 to have different stress regimes and/or different pore fluid states that can locally perturb the fast-axis directions. In addition, the two dominant orientations of the fast polarizations observed from several stations in sectors S1, P2 and F indicate that their fast-axis directions can be affected by nearby faults or/and stress regimes. Gao *et al.* (2019) also reported the two dominant orientations of the fast polarizations in southeastern margin of the Tibetan Plateau and suggested that such scatters can be caused by nearby faults or deep tectonics. Considering that fault orientations

are generally aligned with  $S_{H\max}$  in normal fault regimes such as that in Groningen, the spatial distribution of the fault orientation can also indicate the stress directions. Hence, we sampled the fault orientation from each ray path of the SWS measurements and spatially averaged the samples using the same procedure as that used previously for spatially averaging  $\varphi$  (Fig. 11a). Fig. 11(b) shows the average strike directions and average  $\varphi$  with the difference in their values displayed in the background colours. We found that the fast-axis directions were nearly orthogonal to the fault strike (or expected  $S_{H\max}$ ) in sectors P2-1, P2 and P3.

As we suggest the existence of production-induced fluid flow based on the observation of seasonal peaks in  $\delta tn$  (Fig. 6), fluid flow can be another critical factor that may elucidate the direction of upper crustal anisotropy in Groningen. The modelled fluid flow path at the Groningen reservoir derived through streamline analysis (NAM 2017) shows that the fluid flow predominantly follows the fault geometry, although some flow can be locally perturbed at/near the production wells (Fig. S12). We overlaid the spatial variations of  $\varphi$  derived in this study onto the results of the modelled fluid flow (NAM 2017) for comparison (Fig. S12). The E–W oriented fast-axis directions in sectors P2-1, P2 and P3 are possibly caused by fluid flow towards the nearby extraction wells; the fast-axis directions near the production wells in sectors P2-1 and P2 generally point to the well cluster (Fig. S12). Finally, the complex  $\varphi$  distribution in sector F might be related not only to the complicated fault orientations (Fig. 11a) but also to the sparse and randomized streamline directions (Fig. S12).

## 6.3 Spatiotemporal variation of the anisotropy strength

Fig. 12 shows spatiotemporal distributions of  $\delta tn$  that are computed from the data for each 3-yr incremental period. Although the spatial resolution is limited in this case for the 3-yr period compared with the result for the entire 6 yr (Fig. 4b), the most notable change of  $\delta tn$  is observed at sector P2-1 (Fig. 12). This change can be related to a slight increase in  $\delta tn$  at the production area from 2018 to 2019 (Fig. 6b). The strength of anisotropy in sector P2-1 is possibly increased owing to the changes in gas flow in sector P2-1. Considering that production wells are mostly located in the south

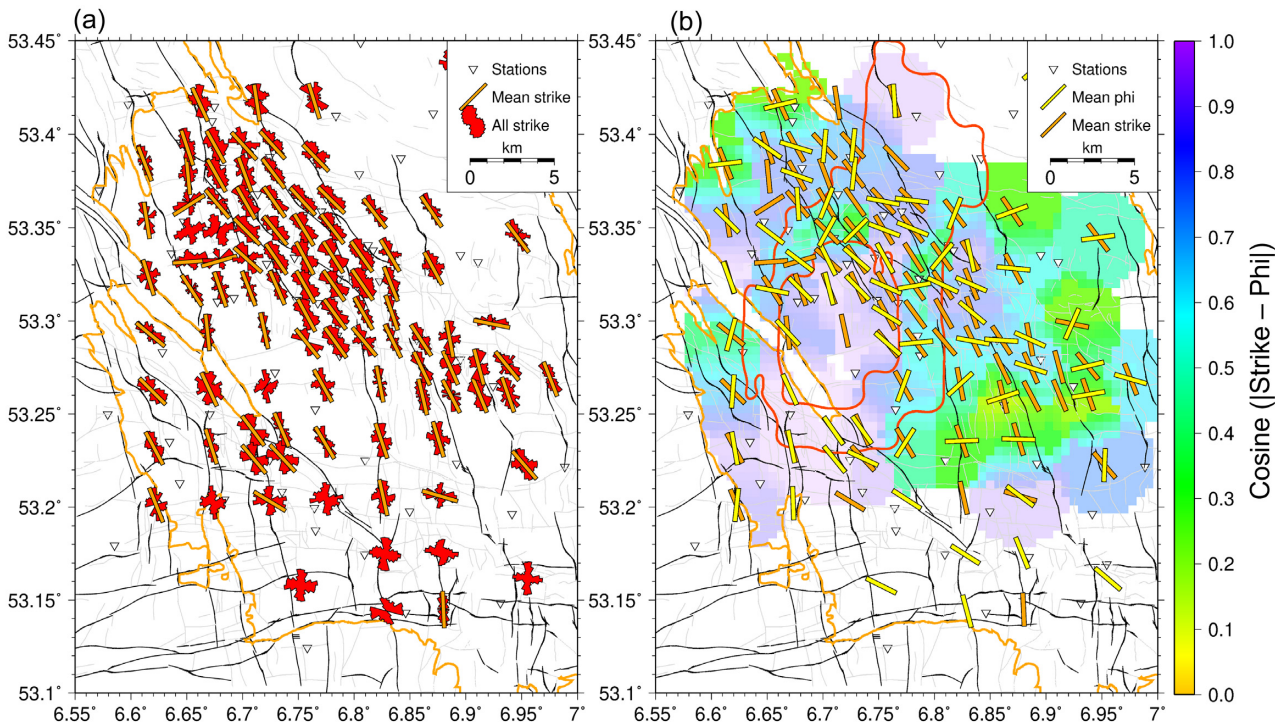


**Figure 11.** Maps showing (a) spatial average of sampled fault strike directions and (b) comparison between the sampled strike direction and  $\varphi$ . Normalized polar histogram of the fault strikes in each grid cell in (a) is shown with red, and the orange bar illustrates the mean direction of the strikes. The mean direction is excluded from plotting if the standard deviation of the strikes in each grid cell exceeds  $25^\circ$ . The background colour in (b) is computed from the absolute value of the cosine of the difference between the strike direction and  $\varphi$ . Orange and yellow bars indicate mean strike and mean  $\varphi$ , respectively. Red contour lines enclose two areas showing the large compaction in the gas field (inner: 0.3 m, outer: 0.25 m).

and central-east of Groningen (Fig. 12f), the direction of gas flow in sector P2-1 can be divided into two: towards the wells in the east and wells in the south (Fig. S12). In this context, a sharp decline in gas production since 2018 may cause this bifurcating flow pattern to a single flow stream, and this single flow stream can potentially increase the number of aligned microcracks, which enhances apparent strength of anisotropy.

Spatiotemporal changes in  $\varphi$  also displayed distinct changes around sector P2-1 (Fig. S13). In sector P2-1 and the central part of sector S1, several  $\varphi$  directions were changed from NW–SE to EW in 2019. This indicates a change in the flow pattern in sector P2-1 from south- and east-flowing streams to a single stream that flows to the east.

#### 6.4 $V_p/V_s$ ratio and null proportion

Microcrack structures of the rocks are important for interpreting seismic velocities and their degree of seismic anisotropy. Microcracks have considerable influence on seismic velocities, especially  $V_p$  (Carlson & Gangi 1985; Kim *et al.* 2019b). For instance, for aligned ellipsoidal cracks, the main reduction in  $V_p$  occurs along the axis of symmetry, leading to significant variations in  $V_p/V_s$  ratio and anisotropy (Anderson *et al.* 1974; Kim *et al.* 2019b, 2020). A microcrack can be empty or filled with fluid at some pore pressure, which can also influence the seismic velocities. For a solid matrix with aligned ellipsoidal fluid-filled cracks, the bulk modulus of the pore fluid in the cracks significantly affects  $V_p$  for a propagation direction along the axis of symmetry (Anderson *et al.* 1974; Kim *et al.* 2019b). Therefore, the distribution of fluid-filled cracks that are aligned by the contemporary stress field causes seismic anisotropy,

leading to shear wave splitting, as our work demonstrated with the case in Groningen.

The  $V_p/V_s$  ratios constrained from various seismological tools can be used to probe variations in seismic wave propagation properties, which are predominantly due to changes in elastic properties of the rocks (e.g. Lucente *et al.* 2010). Thus, the  $V_p/V_s$  ratios can provide critical insights into the presence of fluid in pores or cracks (e.g. Kim *et al.* 2019a). In gas-saturated rock,  $V_p/V_s$  ratio decreases with increasing pore pressure (Vanorio & Mavko 2006); therefore,  $V_p/V_s$  ratio in a gas reservoir is generally maintained at 1.6 or lower (Chatterjee *et al.* 1985). However, as noted earlier, the seismic ray path traverses a large proportion of the upper structures above the reservoir, and these shallow layers tend to have larger  $V_p/V_s$  ratios (Romijn 2017), which results in overestimated  $V_p/V_s$  values in Groningen compared with those from other gas fields. Therefore, we used only the spatial variation of  $V_p/V_s$  ratio, rather than the value itself, for meaningful interpretation.

Within the area involving more or less a constant Zechstein salt layer, we found considerable  $V_p/V_s$  ratio contrast between the area showing the highest compaction (Fig. 5a, contour of 0.3 m compaction) and its surrounding area (Fig. 5a, contour of 0.25 m). Fig. S14 shows modified Wadati diagrams for the two areas considered. While the area with the most compaction shows an average  $V_p/V_s$  ratio of  $2.194 \pm 0.12$  (from 741 samples), its outer area shows the value of  $2.167 \pm 0.14$  (from 674 samples). This difference can be derived from the disparity in the pore fluid pressure of the reservoir. The reduction in the pore-fluid pressure can increase  $V_p$  while the velocity of the fast  $S$  wave remains relatively constant, resulting in elevated  $V_p/V_s$  ratio of the reservoir as the fast  $S$  wave is polarized in the microcrack-aligned direction and less influenced

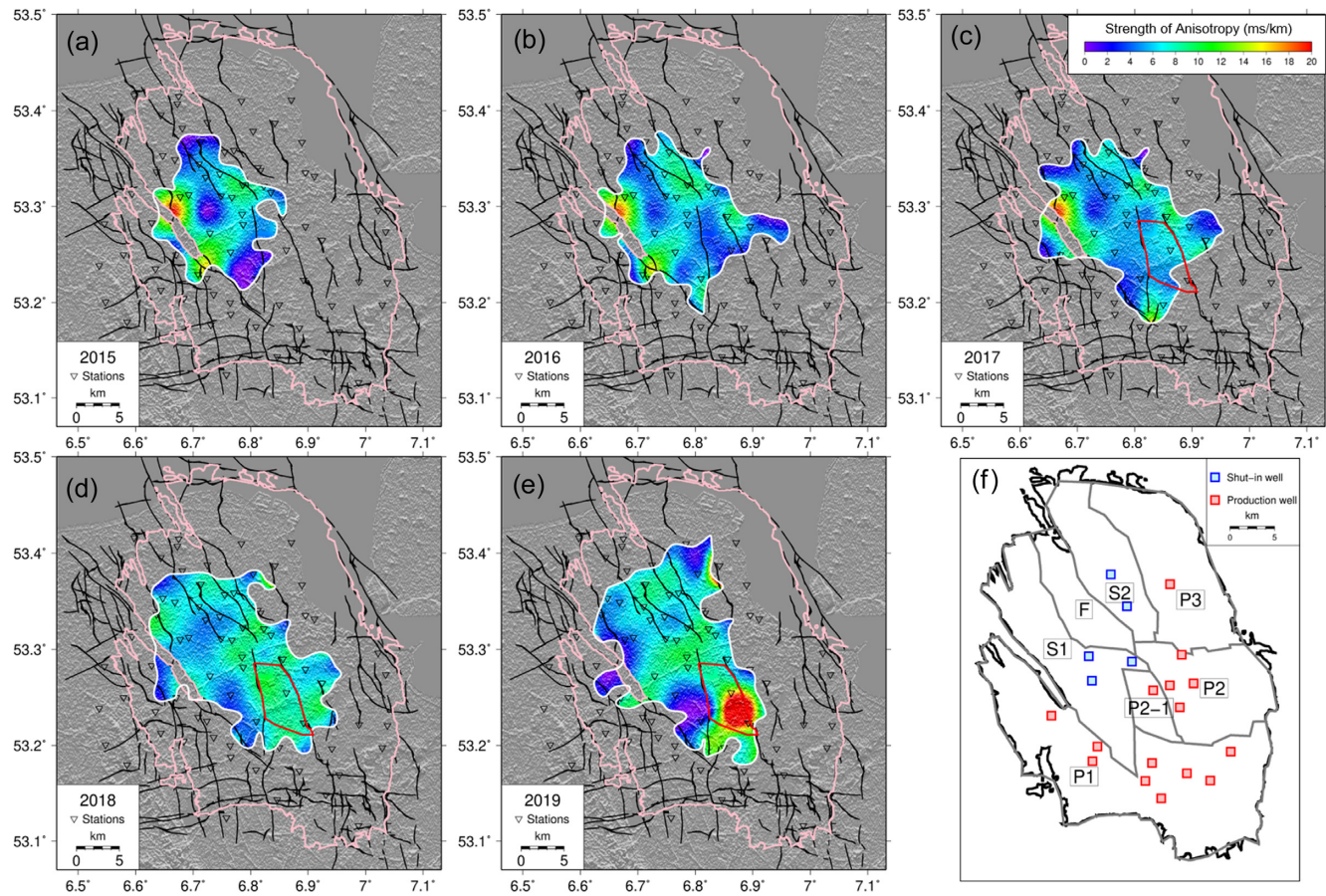


**Figure 12.** Spatiotemporal distribution of  $\delta tn$  for 3-yr period from (a) 2014 to 2016, (b) 2015 to 2017, (c) 2016 to 2018, (d) 2017 to 2019 and (e) 2018 to 2020. Note that the year in each figure legend indicates the second year of the 3-yr period. (f) Compartmentation of the study area by locations of wells and large offset faults. Red contour in (c) and (d) represents sector P2-1 in (f).

by pore pressure changes. Therefore, this pressure drop may impact the largely compacted area. Furthermore, we can determine the relationship between the anisotropic strength and  $V_p/V_s$  ratio. The region where high strength of anisotropy occurs (e.g. sector P2-1) shows a low  $V_p/V_s$  ratio, whereas the region with low strength of anisotropy (highly compacted area) shows a high  $V_p/V_s$  ratio (Fig. 5a). This negative relationship between the two suggests that the dominant pore fluid content of the medium can be gas (Unglert *et al.* 2011).

Typically, it is difficult to interpret the null measurement of SWS because the null occurs in two different circumstances: (1) isotropic null when the  $S$ -wave travels through a nearly isotropic medium (i.e. zero strength of anisotropy) and (2) anisotropic null. In the latter case, a non-split  $S$  wave can be generated in an anisotropic medium when the initial  $S$  wave is polarized parallel to the anisotropic axis (either fast or slow orientations; Savage *et al.* 2010). Although it is nearly impossible to decipher the exact origin of the null from a single measurement with a sufficient data set, it is feasible to constrain the number of isotropic-null measurements. As long as the initial  $S$ -wave directions are randomly distributed, we can ensure that the proportion of anisotropic null is constant in the given data set.

In Groningen, the source mechanisms of induced earthquakes mostly indicate NW–SE trending normal faulting (Willacy *et al.* 2019), and we can thus infer the variation in the null proportion

at each station as that of isotropic nulls. Fig. 5b shows the ratio of nulls to the splitting measurements at each station. Stations in the highly compacted region (Fig. 5b, contour of 0.3 m) generally show a higher null proportion, while stations outside the region show a low proportion. Specifically, the measurements within the highly compacted region showed 54 per cent nulls (291/532), whereas the outer stations showed 47 per cent nulls (238/482). This result agrees with the strength of the anisotropy in this region. The area showing a high strength of anisotropy coincides with the region with a low null proportion, and vice versa. Thus, the null proportion in the SWS can also be used as an indicator of changes in the reservoir.

## 6.5 Anisotropy in the caprock and the sedimentary layer

In this study, we mainly focused on the Rotliegend reservoir to detect spatiotemporal changes in SWS parameters under the assumption that changes in layers above the reservoir, such as Zechstein evaporites and sedimentary basins, would be trivial. Halite-dominated evaporites like Zechstein evaporites can have anisotropy due to lattice preferred orientation by crystal deformation (e.g. Vargas-Meleza *et al.* 2015; Prasse *et al.* 2020). However, in our study area, this effect would be limited. Since the depth of the Zechstein caprock is highly variable (0.2–1 km) in the gas field, their spatial depth variation may follow the pattern of the anisotropy if the layer is significantly anisotropic. Yet, we could not observe any relation-

ship between the salt isopach and the anisotropic pattern (Figs 4 and S14c). Unlike salt layers, upper sedimentary layers (Triassic, Cretaceous and Cenozoic layers) have a nearly constant thickness in Groningen (Strozyk 2017). Considering that faults can exist in upper sedimentary layers in Groningen (van Gent *et al.* 2009), spatial variation in seismic anisotropy in these layers may stem from structure-induced anisotropy. Future work can consider using vertical seismic arrays to quantify the contribution of upper layers in crustal anisotropy at the Groningen gas field.

## 7 CONCLUSIONS

Crustal seismic anisotropy and  $V_p/V_s$  ratio provide useful insights into gas reservoir changes in Groningen. We used shear wave splitting (SWS) methods as well as tomography and spatial averaging methods to probe both spatial and temporal changes in SWS parameters in terms of  $\delta t$  and  $\varphi$ . The data set for the methods includes 3699 waveforms of the induced seismicity, recorded from borehole geophones and surface accelerometers in Groningen from 2014 to 2020. The start of our study period was the time when the Dutch government decided to shut down several production wells, resulting in a stepwise reduction in the overall production rate in the gas field.

Our analysis results indicate that seismic anisotropy in Groningen is strongly related to changes in pore-fluid flow and unequal compaction of the Groningen gas reservoir. The low strength of anisotropy near the shut-in wells is attributed to high reservoir compaction and low fluid flow, leading to fewer aligned fluid-filled microcracks in the reservoir. In contrast, the high strength of anisotropy near the production wells is attributed to low reservoir compaction and a greater number of aligned fluid-filled microcracks, possibly induced by strong fluid flow.

The overall fast-axis direction shows two predominant directions of NNW–SSE and ENE–WSW, which generally agree with the maximum horizontal stress direction of the reservoir. The spatially averaged  $\varphi$  reveals that the fast-axis direction in Groningen is consistent with not only the local stress regime, but also the expected direction of fluid flow. In the spatially averaged  $\varphi$ , the NW–SE direction of  $\varphi$  appears in western Groningen, consistent with the local stress regime, whereas the E–W direction is dominant near the production wells in eastern Groningen, which can be perturbed by fluid flow generated from a strong pressure gradient towards the production well.

Finally, we sampled 1415  $V_p/V_s$  ratios from the central Groningen where the sediment thicknesses are less variable. In this area, we found slightly different  $V_p/V_s$  ratios between largely compacted area (northwest) and less compacted area (southeast). As we compared the  $V_p/V_s$  ratios with the SWS parameters, the observed inverse relationship between  $V_p/V_s$  ratio and the strength of anisotropy indicates that considerable microcracks in the reservoir are unsaturated (i.e. gas-filled). In addition, the spatial distribution of  $V_p/V_s$  ratio and null proportion is both positively related to the amount of reservoir compaction in Groningen. In summary, we constrained several important seismological parameters to provide seismic evidence of fluid flow in Groningen gas reservoir and the potential feasibility of fluid monitoring in the induced seismicity region. We expect our approach to be useful for understanding fluid-induced seismicity and monitoring reservoir pore fluid changes in other regions.

## ACKNOWLEDGMENTS

The authors acknowledge support from the Creative Pioneering Researchers Program of Seoul National University (SNU SRnD 3345–20160014). YK also acknowledges support from National Research Foundation of Korea (NRF) grant funded by the Korean government (MSIT; No. 2022R1A2C1003006). The authors would like to thank Dr Wen Zhou from KNMI for helpful discussion on  $V_p/V_s$  ratio and Dr J. van Elk from NAM for providing the Zechstein isopach map. Seismic data used in this study are obtained from the publicly available Royal Netherlands Meteorological Institute (KNMI) data portal (<http://rds.knmi.nl/dataportal>). Reservoir pressure measured from Static Pressure Gauge (SPG) and monthly gas production rate in Groningen were retrieved from NAM (<https://www.nam.nl/>). All figures in this paper are generated using the GMT (<https://www.generic-mapping-tools.org/>) and Python.

## CONFLICT OF INTEREST

No potential conflict of interest was reported by the authors.

## DATA AVAILABILITY

All data used in this work has been cited.

## REFERENCES

- Anderson, D.L., Minster, B. & Cole, D., 1974. The effect of oriented cracks on seismic velocities, *J. geophys. Res.*, **79**(26), 4011–4015.
- Audoine, E., Savage, M.K. & Gledhill, K., 2004. Anisotropic structure under a back arc spreading region, the Taupo Volcanic Zone, New Zealand, *J. geophys. Res.*, **109**(11), 1–21.
- Boness, N.L. & Zoback, M.D., 2006. Mapping stress and structurally controlled crustal shear velocity anisotropy in California, *Geology*, **34**(10), 825–828.
- Booth, D.C. & Crampin, S., 1985. Shear-wave polarizations on a curved wavefront at an isotropic free surface, *Geophys. J. R. astr. Soc.*, **83**(1), 31–45.
- Bourne, S.J. & Oates, S.J., 2017. Extreme threshold failures within a heterogeneous elastic thin sheet and the spatial-temporal development of induced seismicity within the Groningen Gas Field, *J. geophys. Res.*, **122**(12), 10 299–10 320.
- Bourne, S.J., Oates, S.J. & van Elk, J., 2018. The exponential rise of induced seismicity with increasing stress levels in the Groningen gas field and its implications for controlling seismic risk, *Geophys. J. Int.*, **213**(3), 1693–1700.
- Buijze, L., Van Den Bogert, P.A.J., Wassing, B.B.T., Orlic, B. & Ten Veen, J., 2017. Fault reactivation mechanisms and dynamic rupture modelling of depletion-induced seismic events in a Rotliegend gas reservoir, *Geologie En Mijnbouw/Neth. J. Geosci.*, **96**(5), s131–s148.
- Cao, L., Kao, H., Wang, K., Chen, C., Mori, J., Ohmi, S. & Gao, Y., 2019. Spatiotemporal variation of crustal anisotropy in the source area of the 2004 Niigata, Japan Earthquake, *Bull. seism. Soc. Am.*, **109**(4), 1331–1342.
- Carlson, R.L. & Gangi, A.F., 1985. Effect of cracks on the pressure dependence of P wave velocities in crystalline rocks, *J. geophys. Res.*, **90**(B10), 8675–8684.
- Castellazzi, C., Savage, M.K., Walsh, E. & Arnold, R., 2015. Shear wave automatic picking and splitting measurements at Ruapehu volcano, New Zealand, *J. geophys. Res.*, **120**(5), 3363–3384.

- Chatterjee, S.N., Pitt, A.M. & Iyer, H.M., 1985. Vp/Vs ratios in the Yellowstone National Park region, Wyoming, *J. Volc. Geotherm. Res.*, **26**(3–4), 213–230.
- Cochran, E.S., Li, Y.G. & Vidale, J.E., 2006. Anisotropy in the shallow crust observed around the San Andreas fault before and after the 2004 M 6.0 Parkfield earthquake, *Bull. seism. Soc. Am.*, **96**(4B), S364–S375.
- Crampin, S., 1978. Seismic-wave propagation through a cracked solid: polarization as a possible dilatancy diagnostic, *Geophys. J. R. astr. Soc.*, **53**(3), 467–496.
- Crampin, S. & Chastin, S., 2003. A review of shear wave splitting in the crack-critical crust, *Geophys. J. Int.*, **155**(1), 221–240.
- Crampin, S., Peacock, S., Gao, Y. & Chastin, S., 2004. The scatter of time-delays in shear-wave splitting above small earthquakes, *Geophys. J. Int.*, **156**(1), 39–44.
- Crampin, S. & Peacock, S., 2008. A review of the current understanding of seismic shear-wave splitting in the Earth's crust and common fallacies in interpretation, *Wave Motion*, **45**(6), 675–722.
- De Jager, J. & Visser, C., 2017. Geology of the Groningen field - an overview. *Geologie En Mijnbouw/Neth. J. Geosci.*, **96**(5), s3–s15.
- Dempsey, D. & Suckale, J., 2017. Physics-based forecasting of induced seismicity at Groningen gas field, the Netherlands, *Geophys. Res. Lett.*, **44**(15), 7773–7782.
- Dost, B., Ruigrok, E. & Spetzler, J., 2017. Development of seismicity and probabilistic hazard assessment for the Groningen gas field, *Geologie En Mijnbouw/Neth. J. Geosci.*, **96**(5), s235–s245.
- Dost, B., van Stiphout, A., Kühn, D., Kortekaas, M., Ruigrok, E. & Heimann, S., 2020. Probabilistic moment tensor inversion for hydrocarbon-induced seismicity in the Groningen Gas Field, the Netherlands, Part 2: application, *Bull. seism. Soc. Am.*, **110**(5), 2112–2123.
- Gao, Y., Wu, J., Fukao, Y., Shi, Y. & Zhu, A., 2011. Shear wave splitting in the crust in North China: stress, faults and tectonic implications, *Geophys. J. Int.*, **187**(2), 642–654.
- Gao, Y., Chen, A., Shi, Y., Zhang, Z. & Liu, L., 2019. Preliminary analysis of crustal shear-wave splitting in the Sanjiang lateral collision zone of the southeast margin of the Tibetan Plateau and its tectonic implications, *Geophys. Prospect.*, **67**(9), 2432–2449.
- Hoffman, L.J., Ruigrok, E., Dost, B. & Paulssen, H., 2017. A shallow seismic velocity model for the Groningen area in the Netherlands, *J. geophys. Res.*, **122**(10), 8035–8050.
- Hu, N., Li, Y. & Xu, L., 2020. Crustal seismic anisotropy of the Northeastern Tibetan Plateau and the adjacent areas from shear-wave splitting measurements, *Geophys. J. Int.*, **220**(3), 1491–1503.
- Jagt, L., Ruigrok, E. & Paulssen, H., 2017. Relocation of clustered earthquakes in the Groningen gas field, *Geologie En Mijnbouw/Neth. J. Geosci.*, **96**(5), s163–s173.
- Johnson, J.H., Savage, M.K. & Townend, J., 2011. Distinguishing between stress-induced and structural anisotropy at Mount Ruapehu volcano, New Zealand, *J. geophys. Res.*, **116**(12), 1–18.
- Kim, E., Toomey, D., Hooft, E.E., Wilcock, W., Weekly, R.T., Lee, S.-M. & Kim, Y., 2019a. Upper crustal Vp/Vs ratios of the Endeavour segment, the Juan de Fuca Ridge, from joint inversion of P and S travel times: implications for hydrothermal circulation, *Geochem. Geophys. Geosyst.*, **20**, 208–229.
- Kim, E., Kim, Y. & Mainprice, D., 2019b. GassDem: a MATLAB program for modeling the anisotropic seismic properties of porous medium using differential effective medium theory and Gassmann's poroelastic relationship, *Comput. Geosci.*, **126**, 131–141.
- Kim, E., Kim, Y. & Mainprice, D., 2020. AnisEulerSC: a MATLAB program combined with MTEX for modeling the anisotropic seismic properties of a polycrystalline aggregate with microcracks using self-consistent approximation, *Comput. Geosci.*, **145**, doi:10.1016/j.cageo.2020.104589.
- Kortekaas, M. & Jaarsma, B., 2017. Improved definition of faults in the Groningen field using seismic attributes, *Geologie En Mijnbouw/Neth. J. Geosci.*, **96**(5), s71–s85.
- Kruiver, P.P. *et al.*, 2017. An integrated shear-wave velocity model for the Groningen gas field, The Netherlands, *Bull. Earthq. Eng.*, **15**(9), 3555–3580.
- Li, T., Gu, Y.J., Wang, Z., Wang, R., Chen, Y., Song, T.R.A. & Wang, R., 2019. Spatiotemporal variations in crustal seismic anisotropy surrounding induced earthquakes near Fox Creek, Alberta, *Geophys. Res. Lett.*, **46**(10), 5180–5189.
- Li, Z. & Peng, Z., 2017. Stress- and structure-induced anisotropy in southern California from two decades of shear wave splitting measurements, *Geophys. Res. Lett.*, **44**(19), 9607–9614.
- Licciardi, A., Eken, T., Taymaz, T., Piana Agostinetti, N. & Yolsal-Çevikbilen, S., 2018. Seismic anisotropy in central North Anatolian Fault Zone and its implications on crustal deformation, *Phys. Earth planet. Inter.*, **277**(January), 99–112.
- Lucente, F.P., de Gori, P., Margheriti, L., Piccinini, D., di Bona, M., Chiarappa, C. & Agostinetti, N.P., 2010. Temporal variation of seismic velocity and anisotropy before the 2009 Mw 6.3 L'Aquila earthquake, Italy, *Geology*, **38**(11), 1015–1018.
- Mroczek, S., Savage, M.K., Hopp, C. & Sewell, S.M., 2020. Anisotropy as an indicator for reservoir changes: example from the Rotokawa and Ngatamariki geothermal fields, New Zealand, *Geophys. J. Int.*, **220**(1), 1–17.
- Nederlandse Aardolie Maatschappij, 2013. Technical Addendum to the Winningsplan Groningen 2013, NAM Report, available at: <https://www.tweedekamer.nl/downloads/document?id=4ce3b996-fcb3-4d7b-9fd6-89be7fa10570&title=Technical%20Addendum%20to%20the%20Winningsplan%20Groningen%202013.%20Subsidence%2C%20Induced%20Earthquakes%20and%20Seismic%20Hazard%20An>.
- Nederlandse Aardolie Maatschappij, 2016. Study and data acquisition plan induced seismicity in Groningen-Winningsplan 2016, NAM Report, available at: , accessed October 2021.
- Nederlandse Aardolie Maatschappij, 2017. Groningen Dynamic Model Update 2017, NAM Report, available at: <https://nam-onderzoeksrapporten.data-app.nl/reports/download/groningen/en/d67cb8ac-e5b0-4130-9598-5b7fc83edae2>, accessed October 2021.
- Nederlandse Aardolie Maatschappij, January 29, 2022 Gas-en olie productiecijfers. Retrieved from <https://www.nam.nl/gas-en-olie/gaswinning.html#vanity-aHR0cHM6Ly93d3cubmFtLm5sL2ZlaXRlbil1bi1jaWpmZXJzL2dhc3dpbm5pbmcuaHRtbA=true&iframe=L2VtYmVkL2NvbXBvNlVudC8.aWQ9Z2Fzd2lubmluZw>.
- Nolte, K.A., Tsolfas, G.P., Bidgoli, T.S. & Watney, W.L., 2017. Shear-wave anisotropy reveals pore fluid pressure-induced seismicity in the U.S. midcontinent, *Sci. Adv.*, **3**(12), 1–7.
- Pastori, M., Baccheschi, P. & Margheriti, L., 2019. Shear wave splitting evidence and relations with stress field and major faults from the “Amatrice-Visso-Norcia Seismic Sequence”, *Tectonics*, **38**(9), 3351–3372.
- Peng, Z. & Ben-Zion, Y., 2004. Systematic analysis of crustal anisotropy along the Karadere-Düzce branch of the North Anatolian fault, *Geophys. J. Int.*, **159**(1), 253–274.
- Pickering, M., 2015. An estimate of the earthquake hypocenter locations in the Groningen gas field, Technical Rept., Nederlandse Aardolie Maatschappij BV, available at <https://nam-feitenencijfers.data-app.nl/download/rapport/8b16a9eb-a607-494a-baa5-56e349b6ed0c?open=true>, accessed October 2021.
- Prasse, P., Wookey, J., Kendall, J.M., Roberts, D. & Dutko, M., 2020. Seismic anisotropy in deforming halite: evidence from the Mahogany salt body, *Geophys. J. Int.*, **223**(3), 1672–1687.
- Romijn, R., 2017. Groningen velocity model 2017—Groningen full elastic velocity model September 2017, Technical Rept., NAM report, available at <https://nam-feitenencijfers.data-app.nl/download/rapport/9a5751d9-2ff5-4b6a-9c25-e37e7697bc1?open=true>, accessed October 2021.
- Savage, M.K., Wessel, A., Teanby, N.A. & Hurst, A.W., 2010. Automatic measurement of shear wave splitting and applications to time varying anisotropy at Mount Ruapehu volcano, New Zealand, *J. geophys. Res.*, **115**(12), 1–17.
- Savage, M.K. *et al.*, 2016. Stress, strain rate and anisotropy in Kyushu, Japan, *Earth planet. Sci. Lett.*, **439**, 129–142.
- Silver, P.G. & Chan, W.W., 1991. Shear wave splitting and subcontinental mantle deformation, *J. geophys. Res.*, **96**(B10), 16 429–16 454.

- Smith, J.D., Avouac, J.P., White, R.S., Copley, A., Gualandi, A. & Bourne, S., 2019. Reconciling the long-term relationship between reservoir pore pressure depletion and compaction in the Groningen Region, *J. geophys. Res.*, **124**(6), 6165–6178.
- Smith, J.D., White, R.S., Avouac, J.-P. & Bourne, S., 2020. Probabilistic earthquake locations of induced seismicity in the Groningen region, the Netherlands, *Geophys. J. Int.*, **222**(1), 507–516.
- Spetzler, J. & Dost, B., 2017. Hypocentre estimation of induced earthquakes in Groningen, *Geophys. J. Int.*, **209**(1), 453–465.
- Spica, Z., Perton, M., Nakata, N., Liu, X. & Beroza, G.C., 2018a. Shallow VS imaging of the Groningen area from joint inversion of multimode surface waves and H/V spectral ratios, *Seismol. Res. Lett.*, **89**(5), 1720–1729.
- Spica, Z.J., Nakata, N., Liu, X., Campman, X., Tang, Z. & Beroza, G.C., 2018b. The ambient seismic field at Groningen gas field: an overview from the surface to reservoir depth, *Seismol. Res. Lett.*, **89**(4), 1450–1466.
- Spingos, I., Kaviris, G., Millas, C., Papadimitriou, P. & Voulgaris, N., 2020. Pytheas: an open-source software solution for local shear-wave splitting studies, *Comput. Geosci.*, **134**, doi:10.1016/j.cageo.2019.104346.
- Strozyk, F., 2017. The internal structure of the Zechstein salt and related drilling risks in the northern Netherlands, in *Permo-Triassic Salt Provinces of Europe, North Africa and the Atlantic Margins*, pp. 115–128, Elsevier.
- Tang, C., Rial, J.A. & Lees, J.M., 2005. Shear-wave splitting: a diagnostic tool to monitor fluid pressure in geothermal fields, *Geophys. Res. Lett.*, **32**(21), 1–3.
- Teanby, N.A., Kendall, J.M. & van der Baan, M., 2004. Automation of shear-wave splitting measurements using cluster analysis, *Bull. seism. Soc. Am.*, **94**(2), 453–463.
- Townend, J. & Zoback, M.D., 2001. Implications of earthquake focal mechanisms for the frictional strength of the San Andreas fault system, *Geol. Soc. Spec. Publ.*, **186**, 13–21.
- Townend, J. & Zoback, M.D., 2004. Regional tectonic stress near the San Andreas fault in central and southern California, *Geophys. Res. Lett.*, **31**(15), 1–5.
- Unglert, K., Savage, M.K., Fournier, N., Ohkura, T. & Abe, Y., 2011. Shear wave splitting, vP/vS, and GPS during a time of enhanced activity at Aso caldera, Kyushu, *J. geophys. Res.*, **116**(11), 1–14.
- van Eck, T., Goutbeek, F., Haak, H. & Dost, B., 2006. Seismic hazard due to small-magnitude, shallow-source, induced earthquakes in The Netherlands, *Eng. Geol.*, **87**(1–2), 105–121.
- van Eijs, R.M.H.E., Mulders, F.M.M., Nepveu, M., Kenter, C.J. & Scheffers, B.C., 2006. Correlation between hydrocarbon reservoir properties and induced seismicity in the Netherlands, *Eng. Geol.*, **84**(3–4), 99–111.
- van Eijs, R.M.H.E., 2015. Neotectonic Stresses in the Permian Slochteren Formation of the Groningen Field, NAM Report (EP201510210531).
- van Gent, H.W., Back, S., Urai, J.L., Kukla, P.A. & Reicherter, K., 2009. Paleostresses of the Groningen area, the Netherlands—results of a seismic based structural reconstruction, *Tectonophysics*, **470**(1–2), 147–161.
- van Oeveren, H., Valvatne, P., Geurtzen, L. & Van Elk, J., 2017. History match of the Groningen field dynamic reservoir model to subsidence data and conventional subsurface data, *Geologie En Mijnbouw/Neth. J. Geosci.*, **96**(5), s47–s54.
- van Thienen-Visser, K. & Breunese, J.N., 2015. Induced seismicity of the Groningen gas field: history and recent developments, *Leading Edge*, **34**(6), 664–671.
- van Wees, J.D., Buijze, L., Van Thienen-Visser, K., Nepveu, M., Wassing, B.B.T., Orlic, B. & Fokker, P.A., 2014. Geomechanics response and induced seismicity during gas field depletion in the Netherlands, *Geothermics*, **52**, 206–219.
- van Wees, Jan Diederik, Osinga, S., Van Thienen-Visser, K. & Fokker, P.A., 2018. Reservoir creep and induced seismicity: inferences from geomechanical modeling of gas depletion in the Groningen field, *Geophys. J. Int.*, **212**(3), 1487–1497.
- Vanorio, T. & Mavko, G., 2006. Vp/Vs ratio in gas pressurized saturated sandstones, in *Proceedings of the 2006 SEG Annual Meeting*, OnePetro.
- Vargas-Meleza, L., Healy, D., Alsop, G.I. & Timms, N.E., 2015. Exploring the relative contribution of mineralogy and CPO to the seismic velocity anisotropy of evaporites, *J. Struct. Geol.*, **70**, 39–55.
- Visser, C.A. & Viota, J.L.S., 2017. Introduction to the Groningen static reservoir model, *Geologie En Mijnbouw/Neth. J. Geosci.*, **2017**, 39–46.
- Willacy, C., Van Dedem, E., Minisini, S., Li, J., Blokland, J.W., Das, I. & Droujinine, A., 2019. Full-waveform event location and moment tensor inversion for induced seismicity, *Geophysics*, **84**(2), KS39–KS57.
- Willacy, C., Blokland, J.W. & Van Dedem, E., 2020. Automating event location monitoring for induced seismicity, *Leading Edge*, **39**(7), 505–512.
- Zbinden, D., Rinaldi, A.P., Urpi, L. & Wiemer, S., 2017. On the physics-based processes behind production-induced seismicity in natural gas fields, *J. geophys. Res.*, **122**(5), 3792–3812.
- Zeeuw, Q. & Geurtzen, L., 2018. Groningen dynamic model update 2018, NAM report, available at <https://nam-onderzoeksrapporten.data-app.nl/reports/download/groningen/en/6f04cc4d-ac33-4bc4-909a-2d28817e097a>. Accessed September 2022.
- Zhou, W. & Paulsen, H., 2017. P and S velocity structure in the Groningen gas reservoir from noise interferometry, *Geophys. Res. Lett.*, **44**(23), 11,785–711,791.
- Zhou, W. & Paulsen, H., 2020. Compaction of the Groningen gas reservoir investigated with train noise, *Geophys. J. Int.*, **223**(2), 1327–1337.
- Zinke, J.C. & Zoback, M.D., 2000. Structure-related and stress-induced shear-wave velocity anisotropy: observations from microearthquakes near the Calaveras Fault in Central California, *Bull. seism. Soc. Am.*, **90**(5), 1305–1312.

## SUPPORTING INFORMATION

Supplementary data are available at [GJI](#) online.

**Figure S1.** A summary plot obtained from the manual method for one event as an example. The figure displays raw waveforms (a1–3), bandpass-filtered waveforms (b1–3), polarigrams (c1–3) and particle motions (d1–3). (a1–d1) show a sequence of calculations using the NS- and EW-component waveforms. Similarly, (a2–d2) show results for Fast–Slow (F–S) component waveforms and (a3–d3) for the corrected NS- and EW-component waveforms. ‘Baz’, ‘Epicentral’ and ‘Aoi’ represent the backazimuth, epicentral distance and incidence angle of the event–station pair, respectively. ‘P’ indicates expected initial polarization angle of the S wave.

**Figure S2.** An example showing how the Eigenvalue method works for the same event–station pair used in the manual method (Fig. S1). (a–c) present NS and EW component (denoted as NE), rotated F–S component and corrected waveforms, respectively. (d) Particle motion before the shear wave splitting correction. (e) Particle motion after the correction. (f) Contour plot of the second eigenvalue ( $\lambda_2$ ). The red contour indicates 95 per cent confidence level.

**Figure S3.** A summary plot obtained from the cluster analysis method using the same event–station pair as a comparison to two other methods (Figs S1 and S2). Panel (a) shows  $\delta t$  and  $\varphi$  for each cluster and rejected one, and panel (b) shows selected and rejected clusters as well as window selection. (c)  $\varphi$  Values and their corresponding error bars for different windows. (d)  $\delta t$  values and their error bars for different windows.

**Figure S4.** Plots showing the comparison of results obtained from three different SWS methods. Accepted and rejected parameter values are coloured in blue and orange, respectively. (a–c)  $\varphi$  Values obtained from all three methods, (d–f)  $\delta t$  values obtained from all three methods. (a, d) Comparison of manual and eigenvalue method, (b, e) eigenvalue and cluster analysis method and (c, f) cluster analysis and manual method.

**Figure S5.** Examples showing null splitting measurements for two different methods. (a) A summary plot for the manual method. (b)

A summary plot for the Eigenvalue method. See captions of Figs S1 and S2 for details.

**Figure S6.** Checkerboard test results for the tomographic inversion of  $\delta t$ . (a) Input checkerboard pattern for the synthetic data. (b) Recovered pattern after the inversion. (c) Map showing grid cells used in the inversion, stations (inverted blue triangles), and ray paths (orange lines). The cells covered with more than three ray paths are used in the inversion, and the cells covered with lesser rays (cells coloured in grey) are excluded in the inversion. (d) Residual plot showing the resolution of the model recovered. A green solid line represents residual contour of  $2 \text{ ms km}^{-1}$ .

**Figure S7.** Temporal distribution of  $V_P/V_S$  ratio for the data recorded from the geophones at 200 m depth (light pink circles) and surface accelerometers (light blue circles). (a)  $V_P/V_S$  ratio obtained before correction. (b)  $V_P/V_S$  ratio obtained after correction. Coloured solid lines display  $V_P/V_S$  values that are averaged with 150-d moving window with 15-d step, and dashed lines show their 95 per cent confidence intervals.

**Figure S8.** Spatial averages of  $\varphi$  with different weighting schemes. Normalized polar histogram of  $\varphi$  in each grid box is shown with red. Yellow bar illustrates the mean direction of  $\varphi$ . The mean direction is excluded from plotting if standard deviation of  $\varphi$  in the grid box exceeds  $25^\circ$ . The weighting scheme exploited in this study is as follows: (a) no weighting scheme, (b) weighting inversely proportional to the distance from the node to the station, (c) weighting inversely proportional to the square of the distance from the node to the station, (d) weighting from the 2-D  $\delta t$  tomography results, (e) weighting inversely proportional to the distance from the node to epicentre and (f) weighting inversely proportional to the square of the distance from the node to epicentre.

**Figure S9.** Temporal variation of  $\delta tn$  for the full data catalogue. Red solid line shows a 150-d moving mean value with a 15-d step, and red dashed lines for 95 per cent confidence interval. Grey solid line indicates monthly gas production of the Groningen gas field (NAM 2022).

**Figure S10.** Histogram of  $\varphi$  for stations in Groningen (enlarged from Fig. 10a). (a)  $\varphi$  Values at northern Groningen. (b)  $\varphi$  Values at southern Groningen.

**Figure S11.** Histogram of null measurements for stations in Groningen (enlarged from Fig. 10b). (a) Null values at northern Groningen. (b) Null values at southern Groningen.

**Figure S12.** Streamline map (taken from Fig. 1 in NAM 2017) overlaid with the spatial averages of  $\varphi$  obtained in this study (Fig. 11, yellow bars). Red and blue squares indicate shut-in well cluster and production well cluster, respectively. The map shows expected gas flow at the reservoir, and the streamlines flowing towards different production wells are coloured differently.

**Figure S13.** Spatiotemporal distribution of  $\varphi$  in the period of 2014 to 2020. Mean value of  $\varphi$  is colour-coded with different periods of the data set. Double-headed arrows represent maximum horizontal stress directions as the reference (pink: Zhou & Paulssen 2017, cyan: van Eijs 2015, green: Dost *et al.* 2020).

**Figure S14.** Modified Wadati plot for  $V_P/V_S$  ratio. (a)  $V_P/V_S$  ratio from the events that occurred in the area showing large compaction of the reservoir (Fig. 7a, outer white contour line). (b)  $V_P/V_S$  ratio from the events that occurred in the region outside such area. Colours represent probability density functions (PDFs) estimated from the data points. (c) Zechstein salt isopach in Groningen. We only considered the region enclosed in a black box, showing minimal thickness variation, for computing  $V_P/V_S$  ratios that are shown in (a) and (b).

**Table S1.** Parameters used in Cluster Analysis method (Teanby *et al.* 2004).

**Table S2.** Parameters used in quadtree gridding provided in TESSA (Johnson *et al.* 2011).

Please note: Oxford University Press is not responsible for the content or functionality of any supporting materials supplied by the authors. Any queries (other than missing material) should be directed to the corresponding author for the paper.